Key Points:
- Structural restorations reveal widening of the Hikurangi accretionary wedge by 60 km since 2 ($\pm$ 0.8) Ma
- The low-taper wedge geometry is consistent with a weak and forward propagating megathrust décollement
- Macroscopic thrusting and folding accommodate less than 50% of the total shortening

Supporting Information:
- Supporting Information S1

Correspondence to:
F. C. Ghisetti,
francesca.ghisetti@terrageologica.com

The last 2 Myr of accretionary wedge construction in the central Hikurangi margin (North Island, New Zealand): Insights from structural modeling

Francesca C. Ghisetti[1], Philip M. Barnes[2], Susan Ellis[3], Andreia A. Plaza-Faverola[4], and Daniel H. N. Barker[3]

[1]TerraGeoLogica, Ruby Bay, New Zealand, [2]National Institute of Water & Atmospheric Research, NIWA, Wellington, New Zealand, [3]GNS Science, Lower Hutt, New Zealand, [4]CAGE—Centre for Arctic Gas Hydrate, Environment, and Climate, Department of Geology, UiT the Arctic University of Norway, Tromsø, Norway

Abstract Three depth-converted and geologically interpreted seismic profiles provide a clear image of the offshore outer accretionary wedge associated with oblique subduction of the Pacific Plate beneath the central Hikurangi margin. Plio-Quaternary turbidites deposited over the pelagic cover sequence of the Hikurangi Plateau have been accreted to the margin by imbrication along E-verging thrust faults that propagated up-section from the plate boundary décollement. Growth stratigraphy of piggy-back basins and thrusting of progressively younger horizons trace the eastward advance of the leading thrust front over ~60 km in the last 2 Myr. Moderate internal shortening of fault-bounded blocks typically 4–8 km wide reflects rapid creation of thrust faults, with some early formed faults undergoing out-of-sequence reactivation to maintain critical wedge taper. Multistage structural restorations show that forward progression of shortening involves: (1) initial development of a ~10–25 km wide "proto-thrust" zone, comprising conjugate sets of moderately to steeply dipping low-displacement (~10–100 m) reverse faults; and (2) growth of thrust faults that exploit some of the early proto-thrust faults and propagate up-section with progressive break-through of folds localized above the fault tips. The youngest, still unbreached folds deform the present-day seafloor. Progressive retro-deformations show that macroscopic thrust faults and folds account for less than 50% of the margin-perpendicular shortening imposed by plate convergence. Arguably, significant fractions of the missing components can be attributed to mesoscopic and microscopic scale layer-parallel shortening within the wedge, in the proto-thrust zones, and in the outer décollement zone.

1. Introduction

Accretionary wedge growth at convergent margins involves multiple factors that interact over different time and depth scales. Variations in convergence velocity across the trench, as well as in the mechanical strength of the basal décollement, and the inherited configuration of the subducting slab (e.g., seamounts) arguably exert primary controls on the resulting tectonic evolution [e.g., *von Huene*, 1986; *Graveleau et al.*, 2012]. The thickness and composition of the upper and lower plate units, and thermal and fluid regimes may also influence wedge growth [*Moore*, 1989; *Ellis et al.*, 2015]. Deciphering the deformation of an accretionary wedge thus requires the integration of multiple approaches (e.g., field and laboratory studies, seismic and drilling data, and numerical modeling).

A solid mechanical framework for interpreting the taper geometry of a wedge and the sequence of thrust activation has been provided by geological data on emergent accretionary wedges and by models of critical Coulomb wedges [*Davis et al.*, 1983; *Dahlen*, 1990]. The general tectonic evolution has been reproduced by many analogue and numerical experiments testing the sensitivity to different geometrical and mechanical configurations [e.g., *Colletta et al.*, 1991; *Storti and McClay*, 1995; *Koyi and Vendeville*, 2003; *Schreurs et al.*, 2006; *Yamada et al.*, 2006].

The internal deformation and imbrication of sedimentary rock units in the upper plate have been validated through retro-deformation and kinematic analyses of high-quality 2-D and 3-D seismic reflection data across different margins worldwide [e.g., Nankai, Costa Rica, and Hikurangi, cf. *Morgan et al.*, 1994; *Morgan and Karig*, 1995; *Sitchler et al.*, 2007; *Moore et al.*, 2011; *Burgreen-Chan et al.*, 2015; *Boston et al.*, 2016]. Restoration

techniques help to discriminate between geometrically and kinematically feasible versus unlikely deformation paths, but cannot provide a unique reconstruction of the kinematic history of an accretionary wedge [*Hossack*, 1979]. In particular, one-step restorations from the deformed state to a putative horizontal template ignore the history of progressive strain accumulation and fault propagation, and are not ideal for all cases of syntectonic sedimentation in a growing imbricate wedge, where layers are not deposited on horizontal surfaces, faulting controls sediment thickness, and tectonic rates are faster than sedimentation rates. In these cases, a more informed choice on the deformation sequence is provided by growth stratigraphy controlled by fault propagation and folding, while estimates of timing and rates of shortening depend on a solid chronology of key stratigraphic markers.

Progressive restoration of faulting and folding, together with back-stripping and decompaction of sedimentary units, give important insights on strain accumulation on macroscopic structures, but can only account for a fraction of total shortening when ductile deformation, mass transfer processes, and layer-parallel shortening affect volumetric changes [*Hossack*, 1979; *Mitra*, 1994]. Significant amounts of internal deformation by layer-parallel shortening of soft sediments at the toe of accretionary wedges have been documented by drill cores [*Lundberg and Moore*, 1986; *Morgan and Karig*, 1995] and modeled by lateral variations in seismic velocity controlled by porosity [e.g., *Moore et al.*, 2011]. These studies attribute up to 30–40% of shortening to diffuse, though heterogeneous, distributed strain [*Morgan et al.*, 1994; *Morgan and Karig*, 1995; *Moore et al.*, 2011], compatible with estimates independently derived from field studies and sandbox models [cf. *Koyi*, 1995].

Previous studies show the challenging task of a full reconstruction of the long-term evolution and shortening across an accretionary wedge. In fact, restoring the kinematic history of the inner and deeper thrust imbricates requires an extrapolation of geological interpretations generally beyond the resolution of seismic and outcrop data, and involves a range of brittle to ductile deformation mechanisms. For these reasons, detailed structural restorations are generally possible only for the younger, shallower, and less deformed portions of the accretionary prism [e.g., *Morgan and Karig*, 1995; *Moore et al.*, 2011; *Boston et al.*, 2016]. In contrast, large-scale retro-deformations of the whole accretionary margin [e.g., *Nicol et al.*, 2007; *Burgreen-Chan et al.*, 2015 for the Hikurangi margin] depict snapshots at intervals of several million years, are affected by many uncertainties in the wedge architecture at depth, and may significantly underestimate actual shortening.

Available data for the central Hikurangi margin offer good opportunities for deciphering the progressive deformation history that has controlled the present-day geometry of a wide (>100 km), low taper, sediment-rich accretionary wedge (Figure 1) [*Barker et al.*, 2009; *Barnes et al.*, 2010]. Here, we have analyzed seismic profiles that provide a clear image of the outer thrust faults splaying from the plate interface megathrust, of the growth stratigraphy controlled by progressive thrusting and folding, and of several generations of proto-thrust zones that formed ahead of the migrating deformation front. These profiles provide an excellent template for geological reconstructions of the wedge, though the quality of seismic data and the available inferences on the age of deformed horizons restrict our analysis to the late Pliocene-Quaternary deformation (from 2 ± 0.8 Ma to the present-day). Our study is aimed at: (1) understanding which deformation sequence best accounts for the present-day structural geometry; (2) identifying the early stages of progressive fault growth during accretion of sediments and the deposition of piggy-back basins; (3) quantifying the rate of growth of the accretionary wedge and the component of shortening accommodated by fault imbrication; and (4) detecting possible variations of geometry within the accretionary wedge through time and from north to south.

The new restorations presented in this paper reconstruct, for the first time, progressive steps of synsedimentary deformation of the central offshore Hikurangi accretionary wedge at relatively short time intervals during its late Pliocene-Quaternary evolution (since 2 ± 0.8 Ma). Fault-propagation folding defined by deformed stratigraphic markers and by thickness variations within piggy-back basins allows us to restore several stages of progressive fault growth in the continuously deforming wedge, and to evaluate shortening rates from faulting and folding.

2. Tectono-Stratigraphic Setting of the Study Area

2.1. Regional Tectonic Setting
The Hikurangi accretionary wedge is located above the subducting oceanic Pacific Plate along the eastern margin of North Island, New Zealand and its offshore convergent margin (Figure 1). The subducting plate
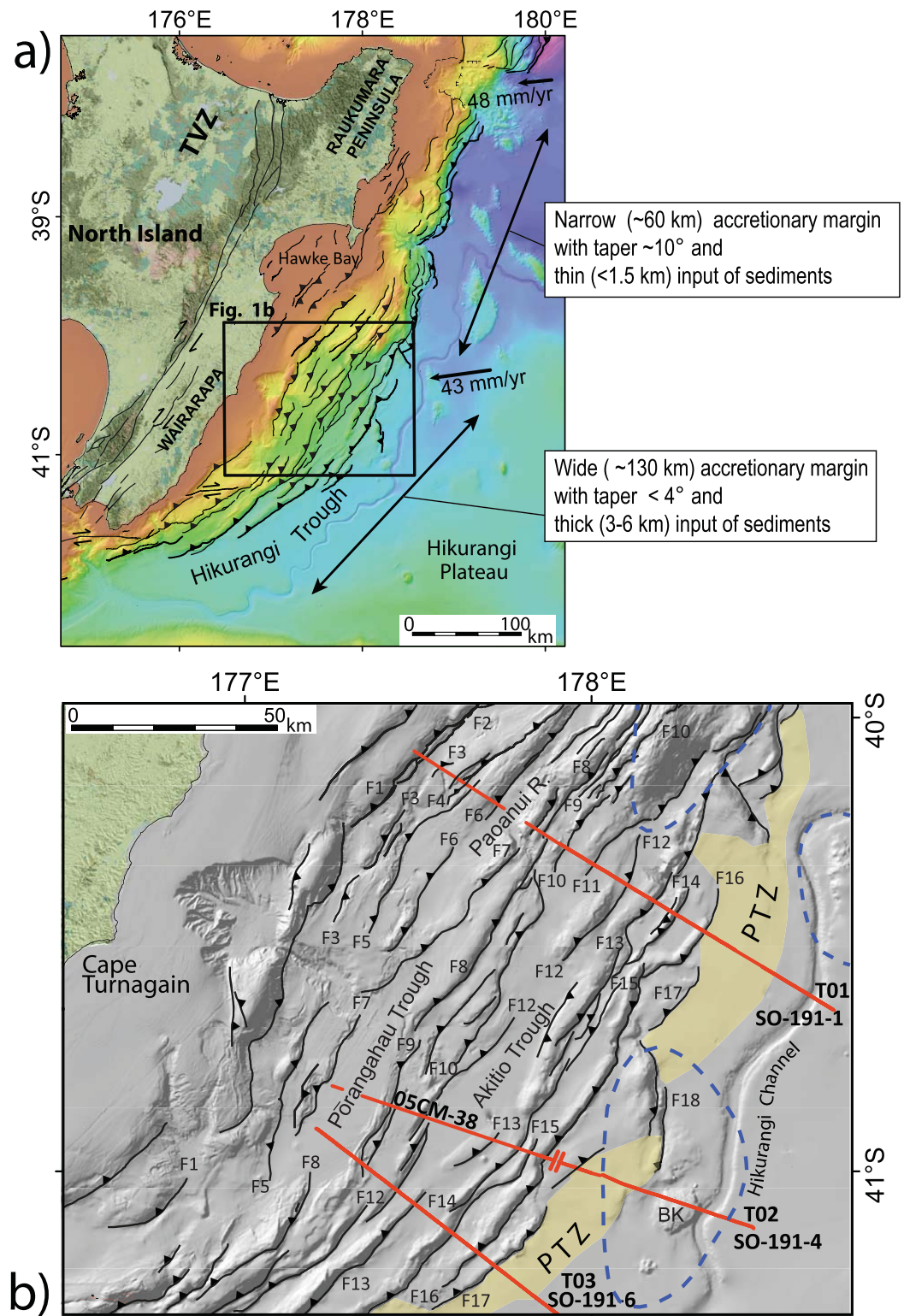
Figure 1. Tectonic setting of the investigated area. (a) Regional setting of the Pacific-Australia subduction zone beneath the North Island of New Zealand. Short black arrows are the vectors of relative motion between the Pacific and Australian plate [*DeMets et al.*, 1994]. TVZ is the Taupo volcanic zone. (b) Location of seismic lines SO-191-1, 05CM-38, SO191-4, and SO191-6 used for construction of the geological Transects T01, T02, and T03 across the central Hikurangi accretionary wedge (see Figures 3–5). Double lines across Transect T02 show the region of overlap between lines 05CM-38 and SO191-4. BK, Bennett Knoll seamount. The dashed blue lines show the base of seamounts on the incoming Pacific Plate (modified from *Barnes et al.* [2010]). Yellow shaded areas are the presently active proto-thrust zones (PTZ). Thrust faults labels are the same in all figures and in the text.

comprises the buoyant Hikurangi Plateau, a large igneous province with crustal thickness of 12–15 km and its sedimentary cover [*Davy et al.*, 2008].

Development of the Hikurangi subduction margin began ~25–20 Ma ago [*Ballance*, 1976; *Cole and Lewis*, 1981; *Lewis and Pettinga*, 1993; *Lamb*, 2011]. Today, thrust-imbricated and strike-slip faulted Cretaceous and Paleogene marine formations emerge above sea-level along the east coast of the North Island [*Pettinga*, 1982; *Beanland et al.*, 1998], whereas the younger Neogene accretionary wedge lies offshore [*Barnes et al.*, 2010]. The southern termination of the subduction margin is currently located in the offshore of northeast South Island, where oblique convergence transforms to the transpressive system of the Marlborough and Alpine faults [*Barnes et al.*, 1998; *Wallace et al.*, 2012].

Along the Hikurangi margin (Figure 1a), the vector of relative motion between the Pacific and Australian plates decreases in magnitude from ~48 mm/yr in the north to ~43 mm/yr southward [*DeMets et al.*, 1994; *Walcott*, 1998; *Beavan et al.*, 2002]. This change involves clockwise rotation of the forearc region and an increase in plate convergence obliquity to the south [*Wallace et al.*, 2004]. These are accompanied by back-arc extension in the Taupo volcanic zone, margin-parallel dextral faulting, and oblique-slip components on thrust faults [*Barnes et al.*, 1998; *Wallace et al.*, 2012].

Morphology, thickness, and composition of the subducting plate change substantially from north to south, with rough topography associated with seamount subduction and trench sediments ~1.0–1.5 km thick in the north and a thick (3–6 km) sedimentary cover in the south [*Lewis et al.*, 1998; *Plaza-Faverola et al.*, 2012]. The morphology of the wedge also changes from being relatively steep (taper angle of ~10°) and narrow (~60 km) in the north to very low taper (<4°) and wide (~130 km) southward (Figure 1a). These differences have been related to changes in strength and fluid overpressure across the wedge [e.g., *Fagereng and Ellis*, 2009; *Wallace et al.*, 2009; *Fagereng*, 2011; *Bassett et al.*, 2014] as well as to a change from frontal tectonic erosion in the north to accretion of the 3–6 km thick sediment apron in the south [*Lewis and Pettinga*, 1993; *Barker et al.*, 2009; *Barnes et al.*, 2010; *Ellis et al.*, 2015]. Arguably, all these differences play a role in controlling shortening modes in the upper plate as well as the observed transition from weak interseismic coupling and steady and episodic seismic creep at shallow depths (<15 km) in the north (Raukumara) [*Wallace et al.*, 2016] and central (Hawke Bay) segments of the margin, to the interseismically locked subduction interface down to depth of 25–40 km in the south (Wairarapa segment). This latter region is thought to fail periodically in large megathrust earthquakes [*Wallace et al.*, 2009].

2.2. Data for the Geological Interpretation of the Study Area

In this study, we construct three geological transects across the central to southern part of the outer Hikurangi margin (Figure 1b), where sedimentary sequences of the incoming Pacific Plate have been accreted to form the outer wedge (Figure 2). Within our study area, the relative motion between the Pacific and Australian plates occurs at a rate of ~43 mm/yr, on an azimuth of about 085°. Kinematic modeling of geological and GPS data indicates that margin-normal convergence rates along this sector of the offshore Hikurangi margin decrease along-strike over a distance of ~80 km from ~40 mm/yr in the north to ~31 mm/yr in the south [*Wallace et al.*, 2004].

The three transects (Figure 1b) are based on seismic reflection lines SO-191-1 (Transect T01), 05CM-38 joined to SO-191-4 (Transect T02), and SO-191-6 (Transect T03). They encompass section lengths of ~85 to 122 km across-strike, and are oriented 125° (T01), 112° (T02), and 131° (T03), i.e., subparallel to moderately oblique to the margin-normal convergence (oriented ~120° in the study region). All transects intersect the strike of the largest thrust faults mapped on the seafloor at angles of 80–90° (Figure 1b).

The seismic profiles used in this study are shown in Figures 3a, 4a, and 5a (see also enlargements in Figures S1, S2, and S3 in the Supporting Information file). Most of these profiles have been partly analyzed in previous studies (e.g., 05CM-38 in *Barker et al.* [2009] and *Wallace et al.* [2009]; SO-191-1 and SO-191-6 in *Barnes et al.* [2010]). The seismic lines from the RV SONNE SO-191 survey were acquired with a source array of 2080 cu. in. volume and short (32 channel) streamer, and display strong seafloor multiples [*Barnes et al.*, 2010]. The short streamer means that detailed velocity information cannot be obtained directly from these data.

In contrast, seismic line 05CM-38 was acquired with a relatively large seismic source array (4140 cu. in. volume) and long hydrophone streamer (12 km/960 channels) [*Barker et al.*, 2009]. In this study, we use a new pre-stack depth migrated (PSDM) version of line 05CM-38, that will be presented in more detail elsewhere by A. Plaza
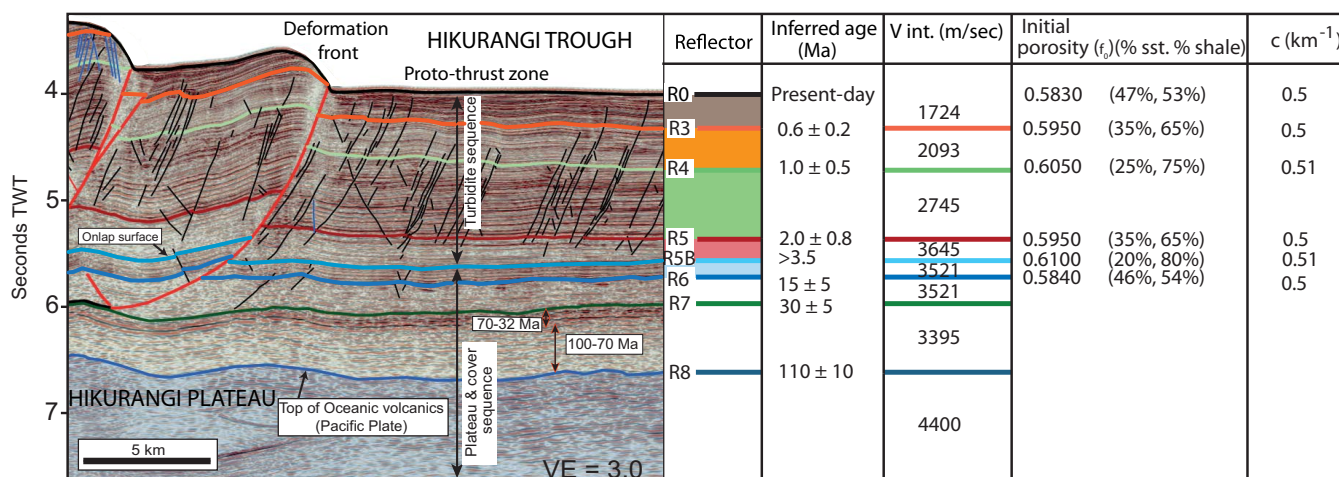
Figure 2. Marker reflectors and units identified in the seismic lines and their assigned age [cf. *Barnes et al.*, 2010; *Plaza-Faverola et al.*, 2012]. The portion of the seismic line shown in this figure is from line SO-191-6 (see Figure 5). Interval velocity (V int.) has been derived from line 05CM-38 PSDM and used for depth conversions of the SO-191 lines (see text). Parameters of initial porosity (f$_0$) and c (rate of change of porosity with depth) have been used for decompaction and back-stripping of units, using the *Sclater and Christie* [1980] relationship. Initial porosity has been calibrated using inferred percentage of sandstone (sst.) and shale in the turbidites from available Holocene sediment cores from the Hikurangi Trough basin floor [*Lewis and Pantin*, 2002] and from onshore data in the Wairarapa region [*Wells*, 1990].

Faverola, D. Klaeschen, I. Pecher, S. Henrys, and L. Wallace (work in progress). The PSDM approach implemented has been already described in *Plaza-Faverola et al.* [2012]. We have used line 05CM-38 PSDM (instead of using the time-migrated line published by *Barker et al.*[2009] and *Wallace et al.* [2009]) because the PSDM of long-offset data yields the most accurate seismic depth section and the best available velocity model.

Major stratigraphic markers used for this study were interpreted in line 05CM-38 PSDM and the interval velocities (V$_{int}$) between markers (Figure 2) were recalculated from the PSDM model taking the average interval velocity over a ∼5 km (400 CDP) region unaffected by deformation at the end of profile 05CM-38, adjacent to the splice with line SO-191-4 (Figure 4). Lines SO-191-1, SO-191-4, and SO-191-6 were then depth converted using the interval velocities derived from line 05CM-38 PSDM.

Depth conversion of line SO-191-4 provides an excellent match for the eastern termination of line 05CM-38 PSDM (Figure 4a). We have no reason to suspect significant variations in the seismic velocities in the region of the trench and toe of the wedge along-strike between transects, and consequently believe that the depth conversions of all the SO-191 data in this toe region are sufficiently accurate. However, the velocity model for the landward portions of the SO-191 lines (inner parts of the wedge) has greater uncertainties, and depth conversion of the SO-191 lines is likely to be less accurate compared to line 05CM-38 PSDM.

We used the décollement depth from transect 05CM-38 PSDM and seismic ties to other 05CM lines at the landward end of line SO-191-1 (e.g., Figure 3 of *Barnes et al.* [2010]) to project the position of the décollement beneath the seafloor multiple on lines SO-191-1 and SO-191-6. The depth uncertainties in the inner reaches of lines SO-191-1 and SO-191-6 do not significantly affect the regional scale interpretation and the retro-deformation analysis, which are the principal goal of this study.

Seismic stratigraphy (Figure 2) in the three transects (Figures 3–5) is similar to that described in *Barnes and Mercier de Lépinay* [1997], *Barnes et al.* [2010], and *Plaza-Faverola et al.* [2012], and has been interpreted accordingly. The sequence of the incoming Pacific Plate comprises the oceanic volcanics of the Hikurangi Plateau below Reflector R8 (Early Cretaceous, equivalent to unit HKB in *Davy et al.* [2008]) and the overlying cover sequence between Reflectors R8 and R5B (Figure 2). This sequence includes a relatively weakly reflective lower unit of possible sandstone-rich sedimentary rocks (unit MES of *Davy et al.* [2008], 100–70 Ma in age), overlain by a strongly reflective unit, interpreted as a condensed sequence of chalk and shales (Sequence Y of *Davy et al.* [2008], 70–32 Ma in age). These units are largely subducted along the margin, while the units above R7 are undergoing accretion.

Above Reflector R7 the upper cover sequence of the incoming Hikurangi Plateau is a weakly reflective interval (R7–R6), overlain by a strongly reflective unit (R6–R5B) (Figure 2). These units are inferred to be nannofossil
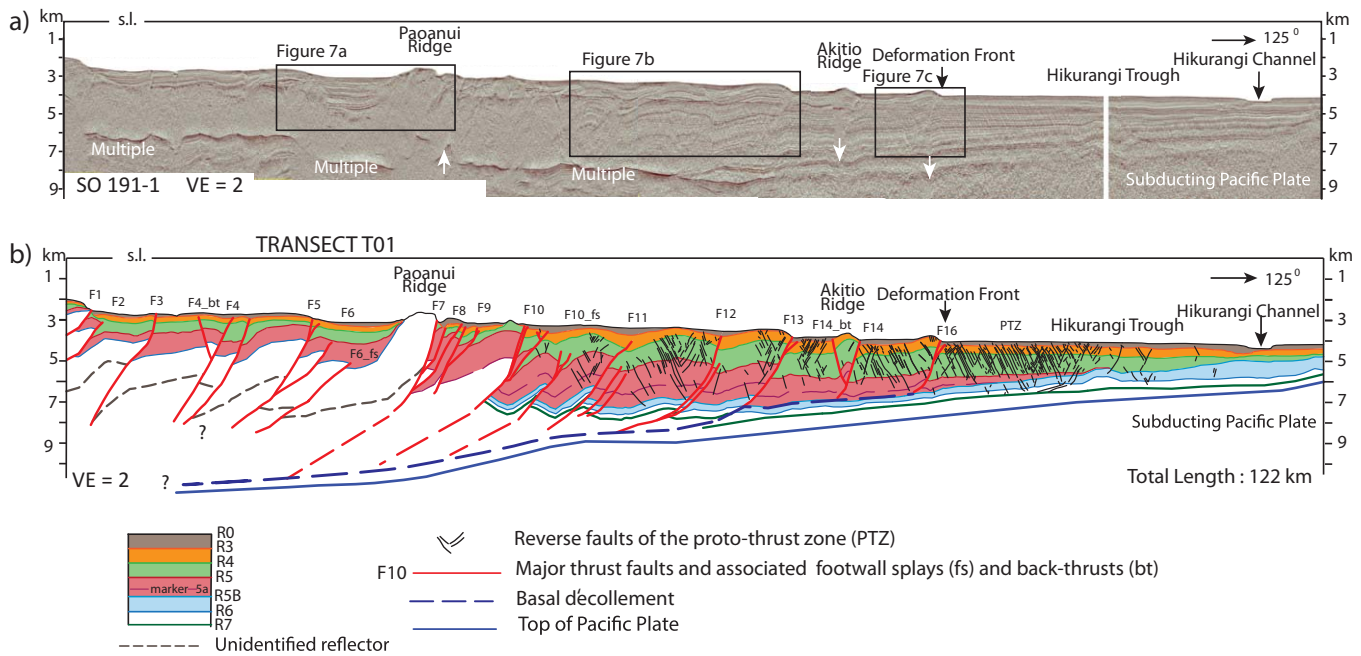
Figure 3. Seismic profile and geological interpretation of Transect T01. (a) Un-interpreted, depth-converted seismic reflection line SO-191-1 (VE = 2, trace in Figure 1b). The white arrows show major artifacts of velocity pull-ups and pull-down that have been smoothed in the geological interpretation. See Figure S1 in the **s**upporting **i**nformation file for enlargement of parts of this line. (b) Interpreted geological Transect T01 shown with the same vertical exaggeration. Marker reflectors and units as in Figure 2. Labels F1–F16 identify thrust faults that can be correlated across the geological transects (cf. Figure 1b) using seafloor bathymetry [*Barnes et al.*, 2010].
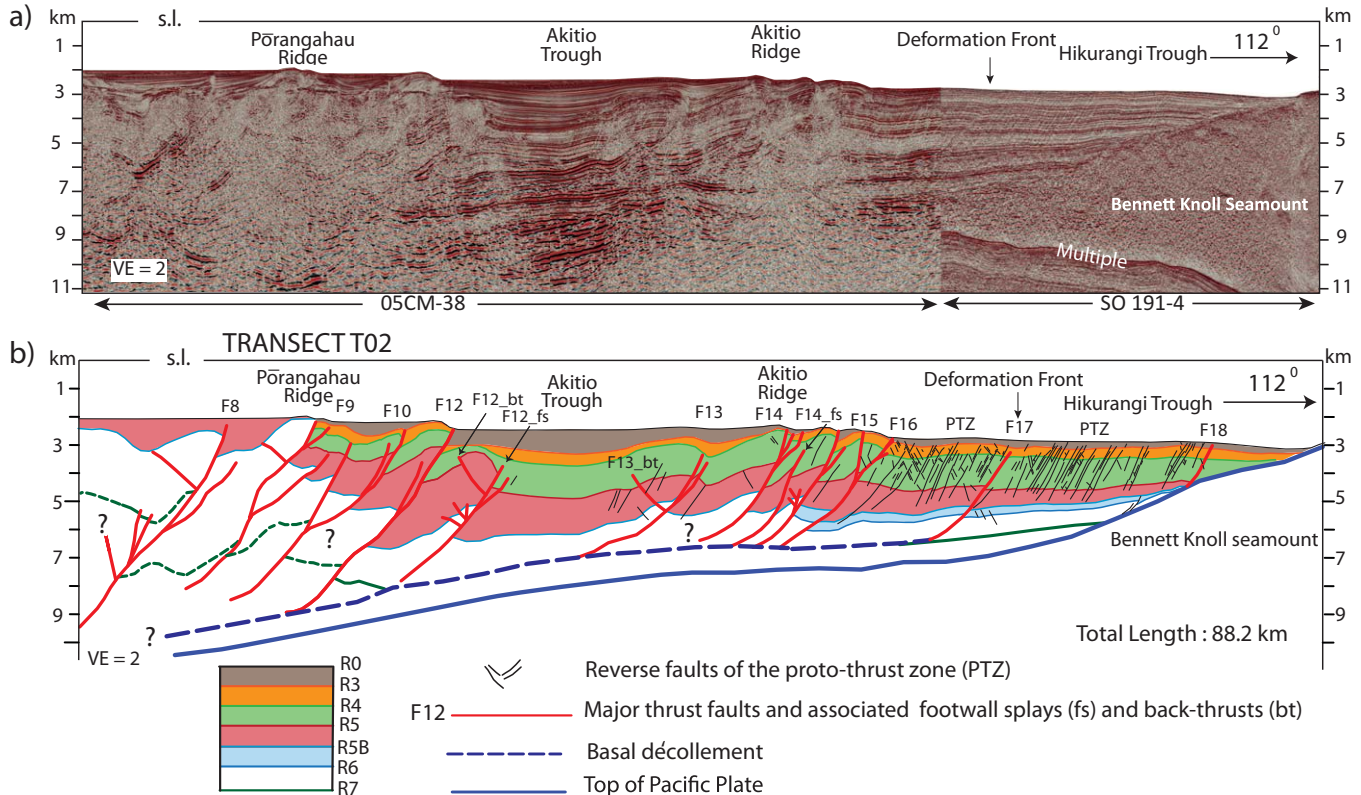
Figure 4. Seismic profile and geological interpretation of Transect T02. (a) Un-interpreted, pre-stack depth migrated (PSDM) line 05CM-38 joined to depth-converted seismic reflection line SO-191-4 (VE = 2, trace in Figure 1b). See Figure S2 in the **s**upporting **i**nformation file for enlargement of parts of this line. (b) Interpreted geological Transect T02 shown with the same vertical exaggeration. Marker reflectors and units as in Figure 2. Labels F8–F18 identify thrust faults that can be correlated across the geological transects (cf. Figure 1b) using sea-floor bathymetry [*Barnes et al.*, 2010].
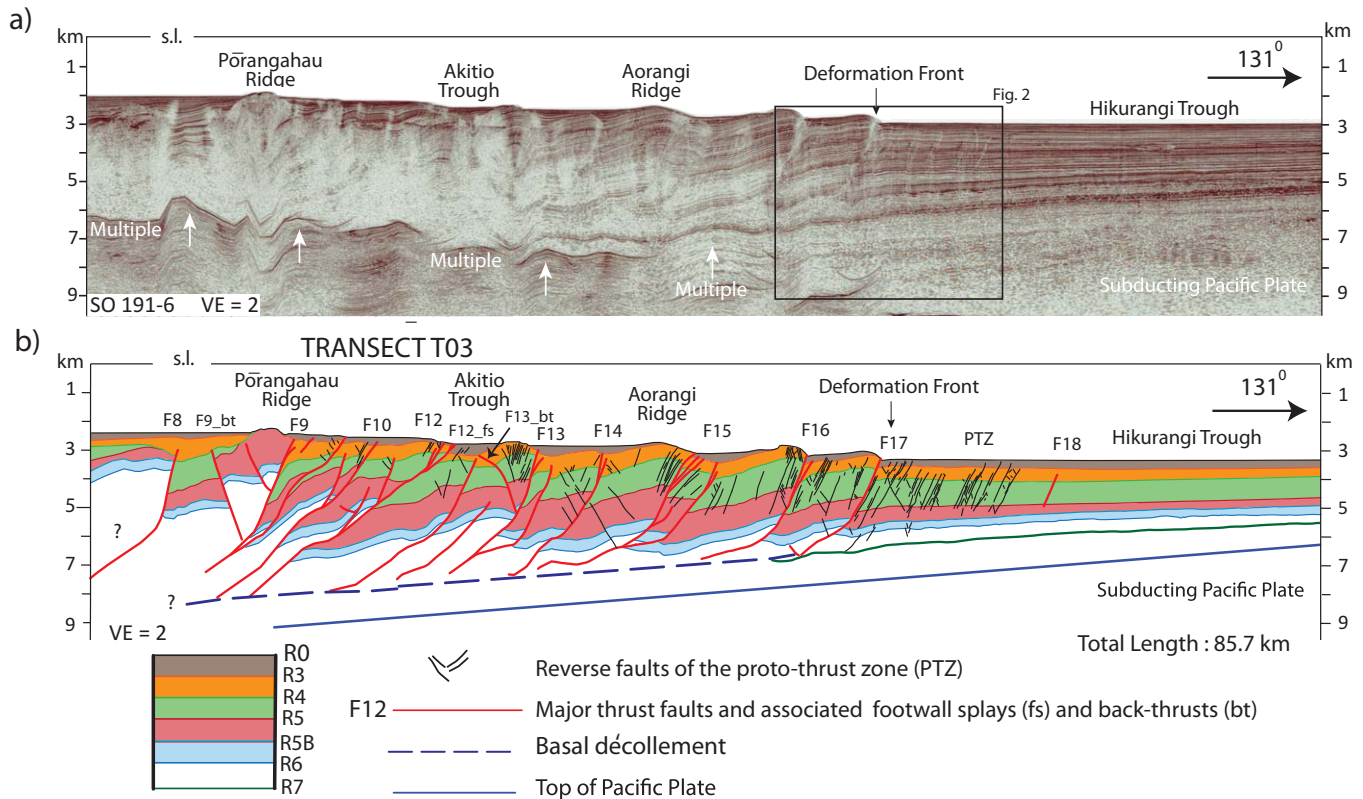
Figure 5. Seismic profile and geological interpretation of Transect T03. (a) Un-interpreted, depth-converted seismic reflection line SO-191-6 (VE = 2, trace in Figure 1b). The white arrows show major artifacts of velocity pull-ups and pull-down that have been smoothed in the geological interpretation. See Figure S3 in the **s**upporting **i**nformation file for enlargement of parts of this line. (b) Interpreted geological Transect T03 shown with the same vertical exaggeration. Marker reflectors and units as in Figure 2. Labels F8–F18 identify thrust faults that can be correlated across the geological transects (cf. Figure 1b) using seafloor bathymetry [*Barnes et al.*, 2010].

chalks interbedded with tephras and clays [*Barnes et al.*, 2010]. Reflector R5B is a regional erosional unconformity associated with westward tilting of the Hikurangi Plateau, overlain by trench turbidites and slope basin sediments [*Lewis and Pettinga*, 1993; *Barnes and Mercier de Lépinay*, 1997; *Lewis et al.*, 1998; *Barnes et al.*, 2010]. In our study region, the thickness of this clastic sequence reaches ∼4 km. Key marker reflectors identified within this sequence (R5, R4, R3, and uppermost Reflector R0 coincident with seafloor) can be traced along the three transects with good confidence, but resolution decreases west of Paoanui and Pōrangahau Ridges (Figures 1 and 3−5), limiting our interpretation to the outer regions of the wedge.

Ages assigned to the reflectors (Figure 2) are not validated by any existing borehole from the Hikurangi Trough, but have been inferred from dated samples at seafloor exposures, and correlated to seismic data from the Hikurangi Plateau east of the trench, tied to ODP site 1124 [*Davy et al.*, 2008; *Barnes et al.*, 2010; *Plaza-Faverola et al.*, 2012]. The sandstone versus shale component inferred for the Plio-Quaternary turbidites (Figure 2) is weakly constrained by Holocene sediment cores from the Hikurangi Trough basin floor [*Lewis and Pantin*, 2002]. Together with outcrop sections in the Wairarapa region [*Wells*, 1990], these values have been used (Figure 2) for calibrating the initial porosity (f_0) and the coefficient of change in porosity with depth (c), used for decompaction [*Sclater and Christie*, 1980, see Section 4]. We cannot quantify the uncertainty on the initial porosities, but we have tested that the results of decompaction during restoration are insensitive to a range of small differences in the chosen parameters.

3. Interpretation of the Geological Transects

The geological interpretation of the seismic lines is shown in Figures 3b, 4b, and 5b. For the northern Transect T01, the quality of seismic data allows us to extend the interpretation to more internal parts of the wedge (thrust fault F1, cf. Figure 1b), though westward of fault F10 we cannot confidently define the
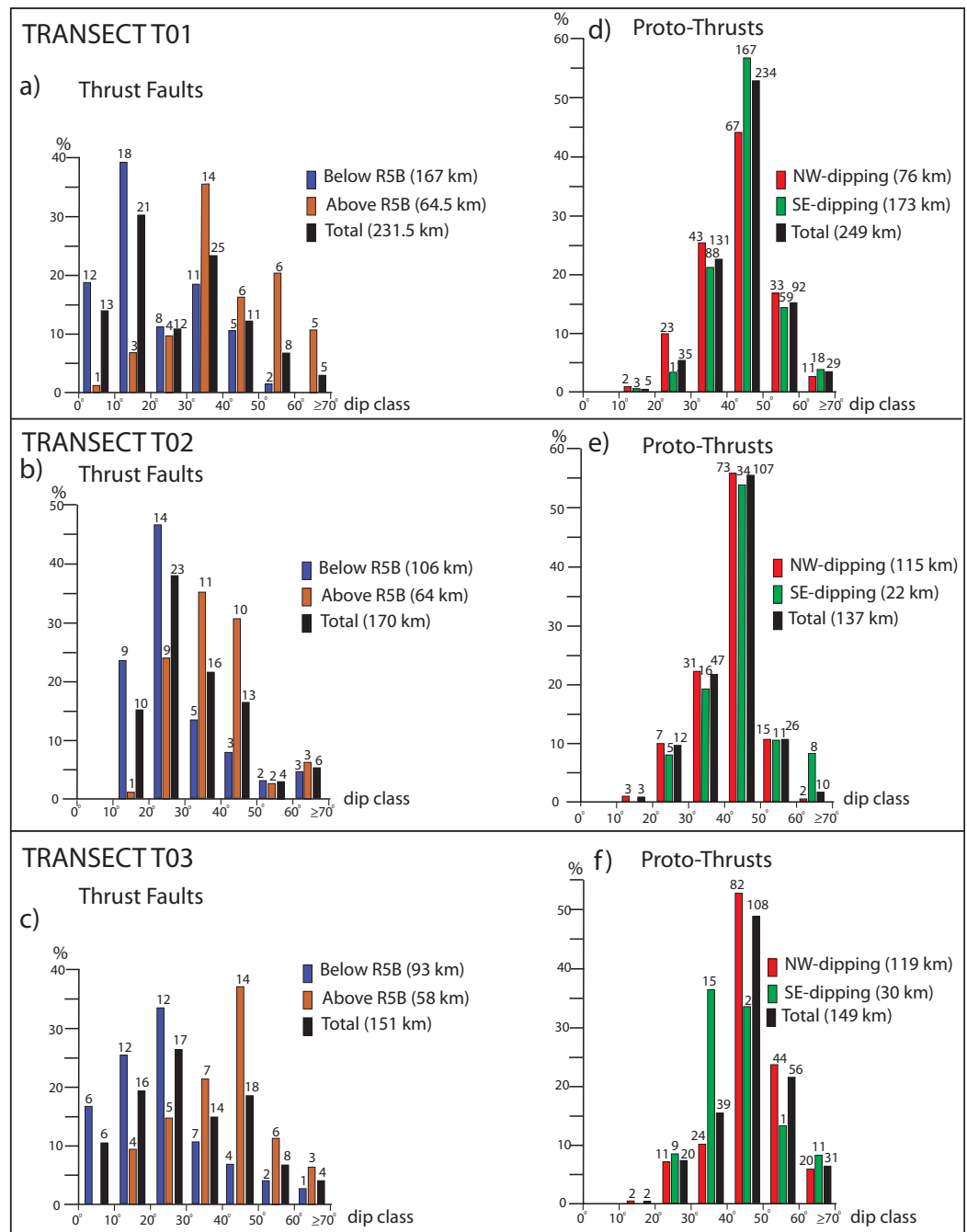
Figure 6. Dip frequency histograms of thrust faults and proto-thrust faults in Transects T01, T02, and T03. Percentage dip distribution is measured in 10° class intervals and weighted over cross-sectional fault length. The number of faults within each class is specified above the columns. (a) Dip frequency of thrust faults in Transect T01. (b) Dip frequency of thrust faults in Transect T02. (c) Dip frequency of thrust faults in Transect T03. Total percentages are compared to percentages for fault segments above and below Reflector R5B. Note that most faults are NW-dipping (see Figures 3b, 4b, and 5b). (d) Dip frequency of proto-thrust faults in Transect T01. (e) Dip frequency of proto-thrust faults in Transect T02. (f) Dip frequency of proto-thrust faults in Transect T03. Total percentages are compared to percentages of SE- and NW-dipping proto-thrust faults.

geometry of units beneath Reflector R5b. For both Transects T02 and T03, our interpretation does not extend beyond thrust fault F8, because of poor seismic resolution west of Pōrangahau Ridge. Given that retro-deformation requires confidence in the stratigraphic correlations across major thrust faults, restorations have been limited to the mid- to outer-slope regions of the three transects, where the late Pliocene-Pleistocene sequence (from R5B to R0) is better resolved.

Individual thrust faults identified in the 2-D transects have been correlated along-strike using their mapped traces on the seafloor (Figure 1b) and are identified by their number in the three transects. The three transects are similar, but show some differences in their structural geometry, as summarized below.

3.1. Thrust Fault Geometry

The plate interface décollement is well resolved beneath the outer slope east of Akitio Trough on all lines (Figure 1b), but is best defined beneath the midslope (west of Akitio Trough) on Transect T02 (compare Figures 3–5). The décollement dips at a low angle of ∼2–3.5° W from a depth of ∼5–6 km in the outermost proto-thrust region to ∼8–10 km beneath the midslope (Figures 3–5). Beneath the outer wedge, the décollement is generally localized along Reflector R7. However, toward the west, the décollement is interpreted to step down locally by >500 m from Reflector R5B beneath thrust fault F13 on Transect T01 and beneath thrust fault F12_fs on Transect T02. In general, the wedge comprises predominantly W-dipping thrust faults, many associated with splays (suffix fs in Figures 3–5). Conjugate back-thrusts (suffix bt in Figures 3–5) are relatively scarce (e.g., F14-bt and F4-bt in T01, F13-bt, and F12-bt in T02, F13-bt, and F9-bt in T03, see Figures 3b, 4b, and 5b, respectively). The taper angle of the wedge (defined as the sum of the surface and basal décollement slopes) varies from ∼3–4° for T01, to ∼4° for T02 and 3.5° for T03.

The geometry of the thrust faults that ramp from the basal décollement has been analyzed in the 2-D transects by measuring the dip of each fault in 10° class intervals (Figure 6). Note that, in Figures 3b, 4b, and 5b, the transects are reproduced with 2:1 vertical exaggeration, and thus the dips appear higher than the true dips. However, the "true" dips (ignoring minor obliquity of the transects relative to individual thrust faults) can be seen in Figures 10e, 11e, and 12e. In order to evaluate the relative distribution of low-angle versus steep fault segments, the dip frequency (Figures 6a, 6b, and 6c) has been weighted over the measured cross-sectional length (rather than the number) of fault segments pertaining to each individual dip class. The dip distribution is bimodal, with predominantly low-angle dips (<30°) beneath R5B and dips in the range 30–50° above it. Steeper faults (dip > 50°) are less frequent (see especially T01). This distribution results from the presence of long fault segments rooting at low dip angles into the basal décollement. Faults commonly have branching splays, with the hanging wall imbricates having higher fault dips than the master fault.

Fault spacing between major faults is variable, typically in the range 3–10 km. The widest spacing occurs in the Pōrangahau and Akitio Troughs (Figure 1b). Transect T02 displays a rather irregular distribution, with close fault spacing (∼3 km) between faults F9–F12 and F16–F14 and a ∼24 km wide interval between faults F12–F14, corresponding with the weakly deformed Akitio Trough (Figures 1b and 4).

3.2. Outer Proto-Thrust Zones

The outermost regions in the transects are characterized by proto-thrust zones up to 25 km wide developed east of the leading deformation front (faults F16 and F17, cf. Figures 3–5). These proto-thrust zones extend beyond the limits of the study area, for an along-strike length of ∼200 km [*Barnes et al.*, 2010]. The proto-thrust zones contain densely spaced sets of low displacement (10–100 m) reverse faults developed across the turbidites deposited on the incoming Pacific Plate. Individual faults cannot be correlated across our three transects, but archived MR1 sidescan sonar data [*Barnes and Mercier de Lépinay*, 1997; *Lewis et al.*, 1998] and recently acquired EM302 bathymetric and backscatter sonar data (NIWA, unpublished data, 2016) indicate they strike subparallel to the major thrust faults. Dip frequency of the proto-thrust faults (Figures 6d, 6e, and 6f) has been analyzed using the same method outlined in section 3.1 for the thrust faults. The histograms show dominant sets of conjugate faults, dipping both landward and seaward at angles of 40–50° (with a second, less dominant set dipping 30–40°). Most faults do not appear to penetrate below Reflector R5B, though we cannot exclude potential loss of seismic resolution with increasing depth.

The eastern boundaries of the proto-thrust zones vary in the three transects. In T01, the densely spaced fabric extends to 17 km east of the deformation front (F16), with sparse proto-thrusts further to the east. In T02, the proto-thrust zone terminates ∼23 km east of the deformation front (F16) against the Bennett Knoll seamount. In T03, the proto-thrust fabric extends ∼10 km east of the deformation front (F17).

West of the primary deformation front, sets of similar, low displacement proto-thrust faults are preserved within other fault-bounded panels. These are notable on Transects T01 (panels between faults F16 and F11) and T03 (panels between faults F17 and F13), where some penetrate the oldest turbidites, down to Reflector R6.
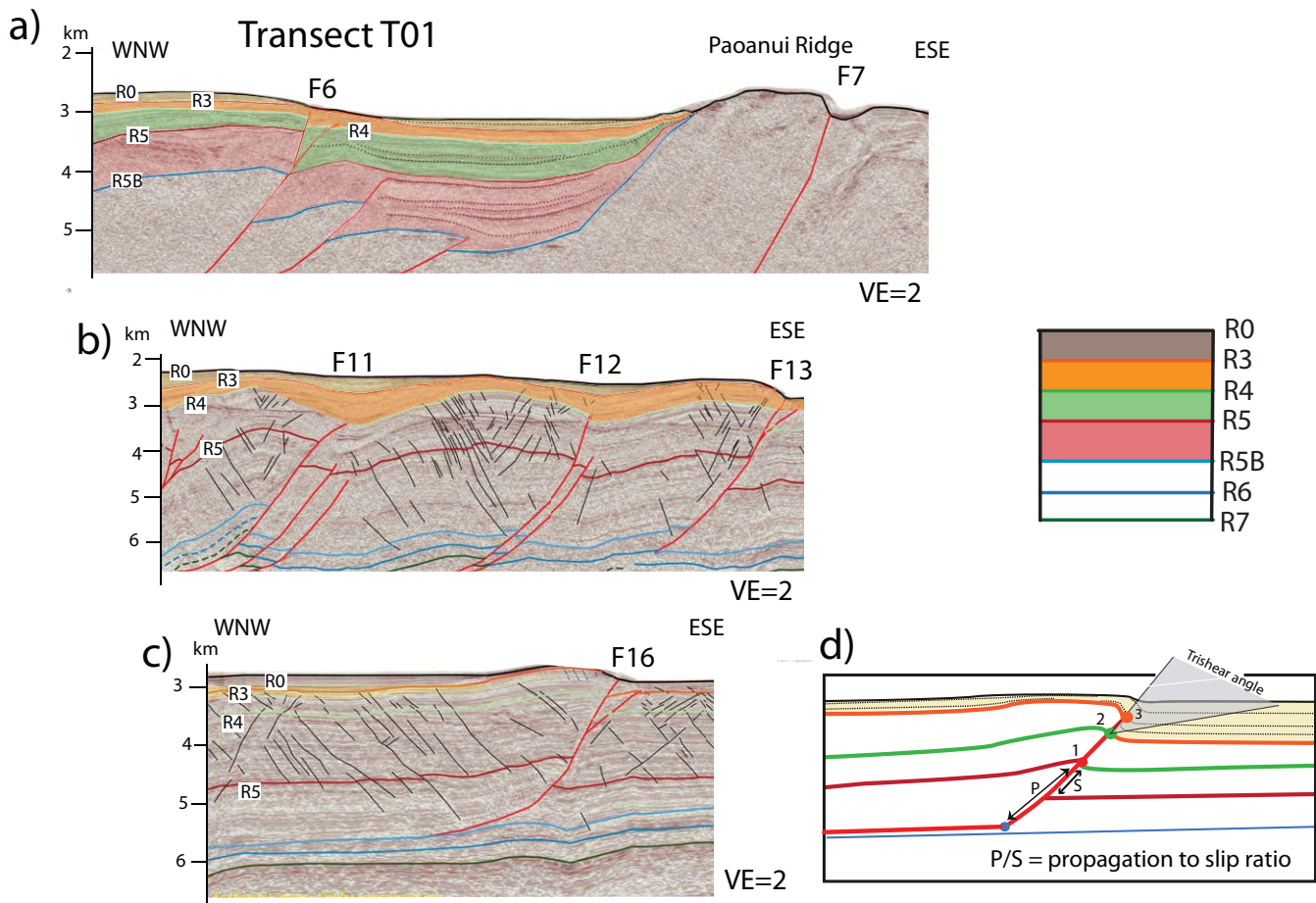
Figure 7. Examples of thrust-controlled growth stratigraphy from Transect T01 (seismic line SO-191-1), showing thickness variations of units of progressively younger age from the inner fault F6 to the outer deformation front F16. See Figure 3a for the location of (a), (b), and (c). Legend of units as in Figures 2 and 3. (a) Growth stratigraphy within units R5B–R5, R5–R4, R4–R3, and R3–R0, all onlapping the western limb of Paoanui Ridge. This geometry is consistent with persistent reactivation of the inner thrust fault F7. (b) Growth stratigraphy within units R4–R3 and R3–R0 for thrust faults F11, F12, and F13, with relative thinning in the hanging wall anticlines and thickening in the footwall synclines. (c) Growth stratigraphy within unit R3–R0, laterally thinning in the hanging wall of fault F16. (d) Forward model of a trishear fault-propagation fold, with three reactivation stages at propagation (P) to slip (S) ratios varying from >2 to ≥1 for a fault tip migrating up-section from the basal décollemet to 1, 2, and 3. The model shows the main parameters of the trishear kinematic model [cf. *Allmendinger*, 1998] and portrays the analogies with fault F16 in Figure 7c (upward decrease in slip, thinning of layers in the hanging wall anticline, and thickening in the footwall syncline within the zone of triangular shear). Forward model prepared using *MOVE* [*Midland Valley*, 2014–2015].

3.3. Growth Stratigraphy

In the three transects, lateral changes in the thickness of units within fault-bounded panels are apparent for the sequence above Reflector R5B. These thickness variations are recorded in the seismic lines by reflection convergence, local onlap and fanning of dips in the limbs of hanging wall anticlines and intervening footwall synclines (see Figure 7 and Figure S1b in the supporting information file for some examples from Transect T01).

Variations in stratigraphic thickness across the thrust wedge relative to the thickness of units in the outer undeformed region of the Hikurangi Trough (east of faults F16 and F17 in T01 and T02 and east of fault F18 in T03) have been measured using the section analysis tool of *MOVE* [*Midland Valley*, 2014–2015] (Figure 8). Because thickness estimation depends on the interpretation of the stratigraphy and on the applied depth conversion, analysis has been limited to the younger stratigraphic sequence R5B to R0 (cf. Figure 2) cut by the outermost faults, where interpretation is robust and structural complexities less significant. Bedding-perpendicular thickness has been measured at intervals of 100 m within the stratigraphic intervals R0–R3, R3–R4, R4–R5, and R5–R5B, and plotted relative to layers restored to a putative horizontal datum in between the major thrust faults (Figure 8).

In each transect, the thickness of stratigraphic units increases landward, but there are also N-S variations in layer thickness (e.g., thicker R4–R5 and R5–R5B intervals in T01 relative to T02 and T03). Significant
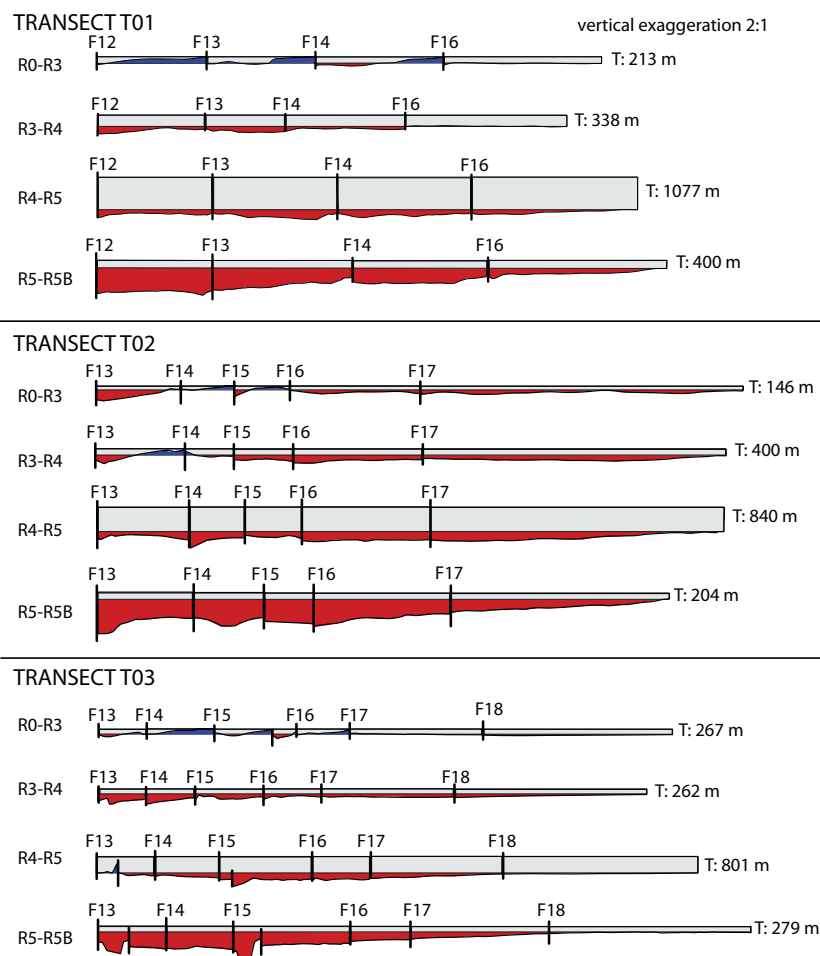
Figure 8. Bedding-perpendicular thickness of units R0–R3, R3–R4, R4–R5, and R5–R5B in Transects T01, T02, and T03. Stratigraphy as in Figure 2. Thickness is measured at intervals of 100 m and plotted for layers restored to a putative horizontal datum in between the thrust faults. Measurements performed using the section analysis tool of *MOVE* [*Midland Valley*, 2014–2015]. Comparison with the thickness (T) of units in the outer zones (gray rectangle) is shown by red areas (excess thickness) and blue areas (thickness deficit). Fault labels as in Figures 3–5. The measurements show the regional westward thickening of units, perturbed by superposed thickness variations adjacent to thrust faults. See text for further discussions.

thickening occurs within the interval R5–R5B, consistent with the wedge-shaped geometry of the sequence onlapping the W-dipping R5B unconformity. Superposed on the general westward increase in thickness there are also changes localized along the major thrust faults. These variations can be attributed to syn-sedimentary thinning of units in the structurally elevated hanging wall sequences, compared to their thickening in the footwall (cf. also Figure 7). These changes are mostly evident within the interval R0–R3 (Figure 8), where units in the fault hanging wall are not only thinner but locally eroded (cf. Figure 7b).

Though our analysis of thickness variations has been limited to the outer wedge faults, the convergent and onlap geometry of reflections on the back limb of hanging wall anticlines that deform the seafloor is also evident for more internal faults beneath the midslope (e.g., faults F6 and F7 in T01; F9, F10, F12 in T02; F8 and F9 in T03, see Figures 3–5, and 7a).

3.4. Fault-Fold Relationships

In all sections, there is a clear association between thrust faults ramping up-section from the basal décollement and geometry of folded units. In Transect T01 (Figure 3b), the hanging wall anticlines of thrust faults F6, F10, F11, F12, F13, and F16 have rounded hinges and long, gently-dipping back-limbs. The footwall synclines are asymmetric, with shorter limbs, axial surfaces pinned to the fault tip, and upward-
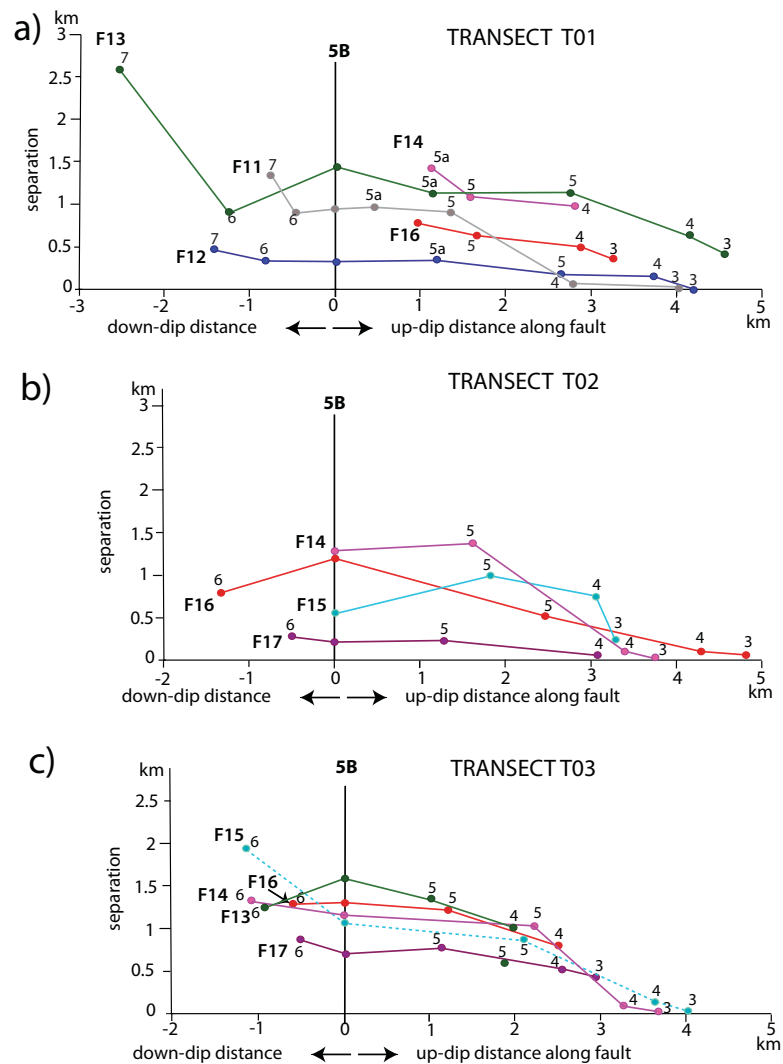
Figure 9. Distance-displacement plots [cf. *Williams and Chapman*, 1983] for the outer faults crossed by the geological transects. (a) Transect T01, (b) Transect T02, and (c) Transect T03. In each plot, reverse separation of marker reflectors (identified by their number 3, 4, 5, 5a, 6, and 7, cf. Figure 2) is plotted against cumulative up-dip distance along the fault. Measurements are normalized relative to Reflector R5B as the origin, with positive separations up-dip from it and negative separations down-dip from it. Individual faults are identified by their number (same as in Figures 3–5) and differentiated by lines with different color and stroke. The data show the general decrease in separation within the sequence above R5B and (or) R5, and more complex separation trends sequence below R5B. See text for further discussions.

shallowing dips in the syntectonic layers. A similar geometry is also observed in Transect T02 (e.g., F12, F12-fs, F13, F14, see Figure 4b) and T03 (e.g., F14, F15, F16, F17, see Figure 5b).

In most cases, there is a decrease in displacement toward the fault tip, with unbreached folds above it (cf. Figure 7 for some examples from Transect T01). This decrease in displacement is shown for the major faults in each transect (Figure 9) by distance-displacement plots [cf. *Williams and Chapman*, 1983; *Hughes and Shaw*, 2014, 2015]. On these plots, the separation of marker horizons across the fault is measured and plotted versus cumulative distance up the fault. All measurements have been normalized relative to Reflector R5B as the origin, with positive separation up-dip from it and negative separation down-dip from it. The plots show significant variations between individual faults in each transect and between the three transects, but in many cases the separation decay within the sequence above R5B (and/or R5) shows a linear trend, though with different slopes. In contrast, more complex separation trends occur in the sequence below R5B, and, for some faults, separation decreases (or remains similar) from R5b to R6 (e.g., faults F11, F13 in T01, F16 in T02, F13 in T03). The largest separation across Reflector R5B is generally 1–1.5 km and decreases to values of few tens/hundred meters across Reflector R3.

4. Progressive Retro-Deformation of the Geological Transects

4.1. Restoration Sequence Reconstructed from Growth Stratigraphy and Kinematic Models of Fault Propagation Inferred From Fault-Fold Relationships

Growth stratigraphy (Figures 7 and 8) provides a very sensitive marker for development and timing of structural relief following the onset of faulting and folding. Growth stratigraphy associated with shortening of layers is most notable within the sequences R4–R3 (from 1.0 ± 0.5 to 0.6 ± 0.2 Ma) and R3–R0 (from 0.6 ± 0.2 Ma to present-day) but it occurs locally also within the sequence below R5 (2 ± 0.8 Ma).

The presence of unbreached folds above blind fault tips, up-dip decreases in fault displacement (Figure 9), and syn-tectonic thickening of layers in fault footwalls are all diagnostic of fault-propagation folding [*Shaw et al.*, 2005]. Such observations have been made in many fold-and-thrust belts and accretionary prisms worldwide [e.g., *Brandes and Tanner*, 2014]. A number of kinematic models (e.g., detachment fold, fault-bend fold, trishear fault-propagation fold) can be used to reproduce folding accommodating the decrease of slip at the tip of a propagating fault [*Hughes and Shaw*, 2015]. However, the structures produced by these models are end members of a continuum, principally controlled by the fault dip and its geometry (e.g., staircase trajectory for a fault-bend fold versus fault propagation along a low-angle décollement for a detachment fold) as well as by different values of fault propagation (P) versus fault slip (S) [*Allmendinger et al.*, 2004]. Given that the parameter P/S can be specified and changed when using the trishear algorithm in restoration softwares (e.g., MOVE [*Midland Valley*, 2014–2015]), this kinematic model provides a versatile tool for restoring (or forward modeling) a wide range of geometries associated with fault-propagation folding. In our three transects, the presence of: (1) folds with smooth profiles and rounded anticlinal hinges; (2) upward-shallowing dips in the footwall synclines; (3) concave geometry of faults ramping up-section with no staircase trajectory; and, (4) upward decrease in displacement from Reflector 5B upward, are all elements consistent with trishear fault-propagation folding [*Erslev*, 1991; *Allmendinger*, 1998; *Hughes and Shaw*, 2014, 2015]. Linear trends in the up-dip separation decrease that we observe for our faults (Figure 9) are indeed typical of fault-propagation folding kinematics. In the case of trishear faulting, the slope of the linear trend is controlled by the fault dip and by the propagation (P) to slip (S) ratio [cf. *Hughes and Shaw*, 2014, 2015]. Slope variations in the linear decrease of fault separation observed in our three transects (Figure 9) can be modeled by changing the propagation to slip ratio (P/S) during fault growth across the stratigraphic sequence. A forward model of a trishear fault propagating above R5B with $1 \leq P/S \leq 2$ accurately reproduces (see Figures 7c and 7d) the geometry of the syntectonic fold in the hanging wall of F16 in Transect T01. It also reproduces the growth stratigraphy of the R4–R3 sequence within a triangular zone of distributed penetrative shear in front of the fault tip [cf. *Hardy and Ford*, 1997; *Brandes and Tanner*, 2014]. For Transects T01, T02, and T03, restoration of fault-propagation folds in different position in the wedge has been achieved using P/S parameters generally in the range 1–5, and in few cases >10 (cf. Figures S4–S13 in the supporting information file).

The youngest stages of fault-propagation folding are apparent in the deformation of the seafloor above an upward propagating fault tip in T01 (faults F16, F14, F13, F10, and F7 in Figure 3b), T02 (faults F16, F14, F12, and F9 in Figure 4b) and T03 (faults F17, F16, F15, F13, F12, and F9 in Figure 5b). These are consistently indicated by linear distance-displacement plots for the outermost fault (e.g., F16 in T01, T02, T03; F17 in T02 and T03, cf. Figure 9). However, identification of earlier stages of fault-propagation folding is difficult, because of the breaching of folds by faults ramping up-section with steeper dips above Reflector R5 (Figure 6). This process changes the geometry of the folded layers, and may explain more complex relationships in the distance versus displacement plots of the inner thrust faults relative to the outer ones (Figure 9).

4.2. Restoration Workflow

The analysis of the structural geometry summarized in section 4.1 provides the rationale for progressive 2-D retro-deformation of the geological transects (performed using MOVE [*Midland Valley*, 2014–2015]), by: (1) constraining the relative timing and sequence of propagation of the major thrust faults based on their control on growth stratigraphy of the units between Reflectors R5B–R0; and (2) defining trishear fault-propagation folding as a suitable kinematic model for interpreting the geometry of layers folded above the fault tips, and for restoring fault separation that decreases up-section.

Restorations presented in this paper (Figures 10–12) differ substantially from those attempted at an earlier stage of our analysis [*Barnes et al.*, 2014]. In our early attempts (Figure S14 in the supporting information file),
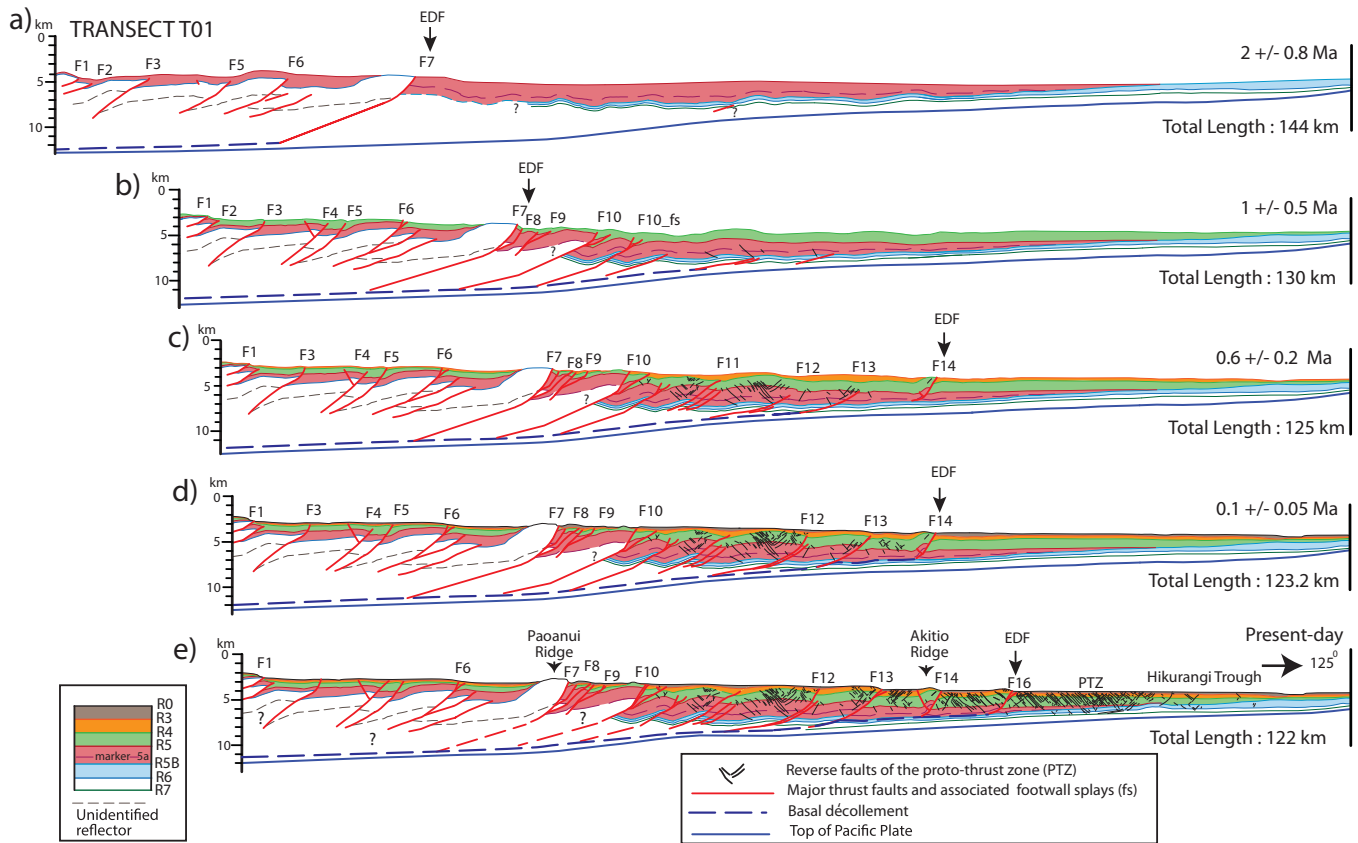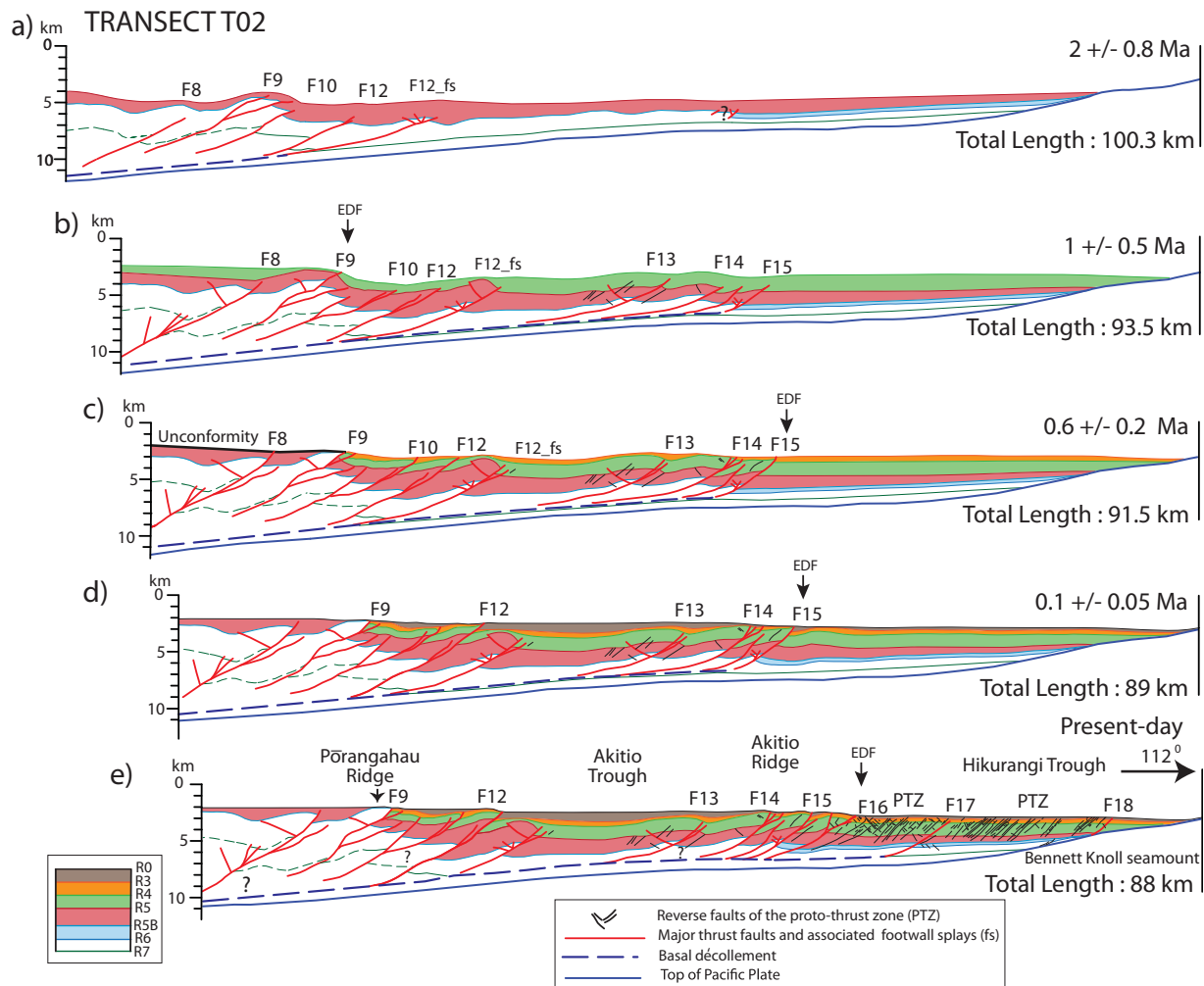
Figure 10. Progressive retro-deformation of Transect T01. (a) Reconstruction at the end of deposition of the sequence below Reflector R5. (b) Reconstruction at the end of deposition of the sequence below Reflector R4. (c) Reconstruction at the end of deposition of the sequence below Reflector R3. (d) Reconstruction during deposition of the sequence R3–R0. (e) Present-day geometry. No vertical exaggeration. Only faults active at each stage are identified by their number. EDF is the emergent deformation front at each stage. See text for details.

we adopted kinematic models of oblique and fault-parallel simple shear [cf. *Groshong*, 2006] for restoring fault separation and then unfolded the markers to a putative paleo-bathymetry of the seabed. These reconstructions are unsatisfactory because they assume that marker horizons originally deposited along a planar datum were first folded and then faulted, in contrast to the evidence of progressive seaward migration of deformation and syn-sedimentary fault growth. These assumptions fail to reproduce the geometry and thickness variations of growth stratigraphy and also result in geometric inconsistencies, as detailed in Figure S14 in the supporting information file.

The strength of the trishear restoration workflow adopted in this paper is the kinematic link between development of folds and forward propagation of thrust faults through time. This workflow makes it possible to reproduce the creation (or destruction) of space controlled by syn-sedimentary folding while maintaining the lateral variations in sedimentary thickness. The trishear kinematic model achieves good results in progressively flattening the layers once fault separation is restored, though some components of folding remain in the lower wedge sequence (i.e., R5B–R6, cf. Figures 10a, 11a, and 12a). It is possible that early stage folding of the sequences involved components of layer-parallel shortening that are not modeled by trishear and/or that the geometry of natural folds is affected by mechanical heterogeneities of the layered sequence that cannot be modeled using geometric restorations. Note also that, though admissible, the sections cannot be fully balanced because the syntectonic units (from R5 to R0) do not have layer-cake stratigraphy, nor were they originally deposited on a regional horizontal datum. Other factors affecting area changes within the sections are caused by submarine erosion of anticlinal crests, accompanied by mass transport away from the plane of the section. Moreover, potential components of oblique thrusting cannot be ruled out, as the sections are not exactly parallel to the shortening direction (cf. Figure 1), with an obliquity of ∼5° for T01 and ∼10° for T02 and T03.

The following workflow has been employed for the reconstructions presented in Figures 10–12 and is described in further details in Figures S4–S13 of the supporting information file.

Figure 11. Progressive retro-deformation of Transect T02. (a) Reconstruction at the end of deposition of the sequence below Reflector R5. (b) Reconstruction at the end of deposition of the sequence below Reflector R4. (c) Reconstruction at the end of deposition of the sequence below Reflector R3. (d) Reconstruction during deposition of the sequence R3–R0. (e) Present-day geometry. No vertical exaggeration. Only faults active at each stage are identified by their number. EDF is the emergent deformation front at each stage. See text for details.

1. Removal of deformation above the basal décollement in progressive steps from the present-day (deformed seafloor R0) backward (to R5), with recovery of fault separations. Faults active during deposition of the sequence bounded by the marker units (R0–R5) are identified by their offset of the marker beds and/or their control on growth stratigraphy during each depositional interval (R0–R3, R3–R4, R4–R5). Faults active during each retro-deformation interval are identified by their relative number in Figures 10–12. For each restoration step, the proto-thrusts ahead of a major thrust fault are removed first; then deformation is removed within individual fault-bounded blocks, from the outer zones inward. For all faults with evidence of associated fault-propagation folding retro-deformation uses trishear kinematics, with progressive flattening of the hanging wall anticline and footwall syncline in the syntectonic sequence. The most important parameters needed for trishear restoration are displacement, trishear angle and propagation to slip ratio (P/S) [cf. *Allmendinger*, 1998; *Allmendinger et al.*, 2004] (see also Figure 7d). The values chosen for each fault are those that achieve (by trial and error) the best retro-deformation of folding and fault offset. Once fault separation and associated folding are recovered, the fault is removed. Where fault-propagation folding is not evident or in the case of faults with small displacement (e.g., proto-thrust faults) restoration of fault separation has been achieved using kinematic models of oblique simple shear and fault-parallel shear [cf. *Gibbs*, 1983; *Groshong*, 2006].

2. Restoration of faults active during deposition of each sequence (R0–R3, R3–R4, and R4–R5) is followed by decompaction and back-stripping of the respective sequence, using the *Sclater and Christie* [1980] relationship:
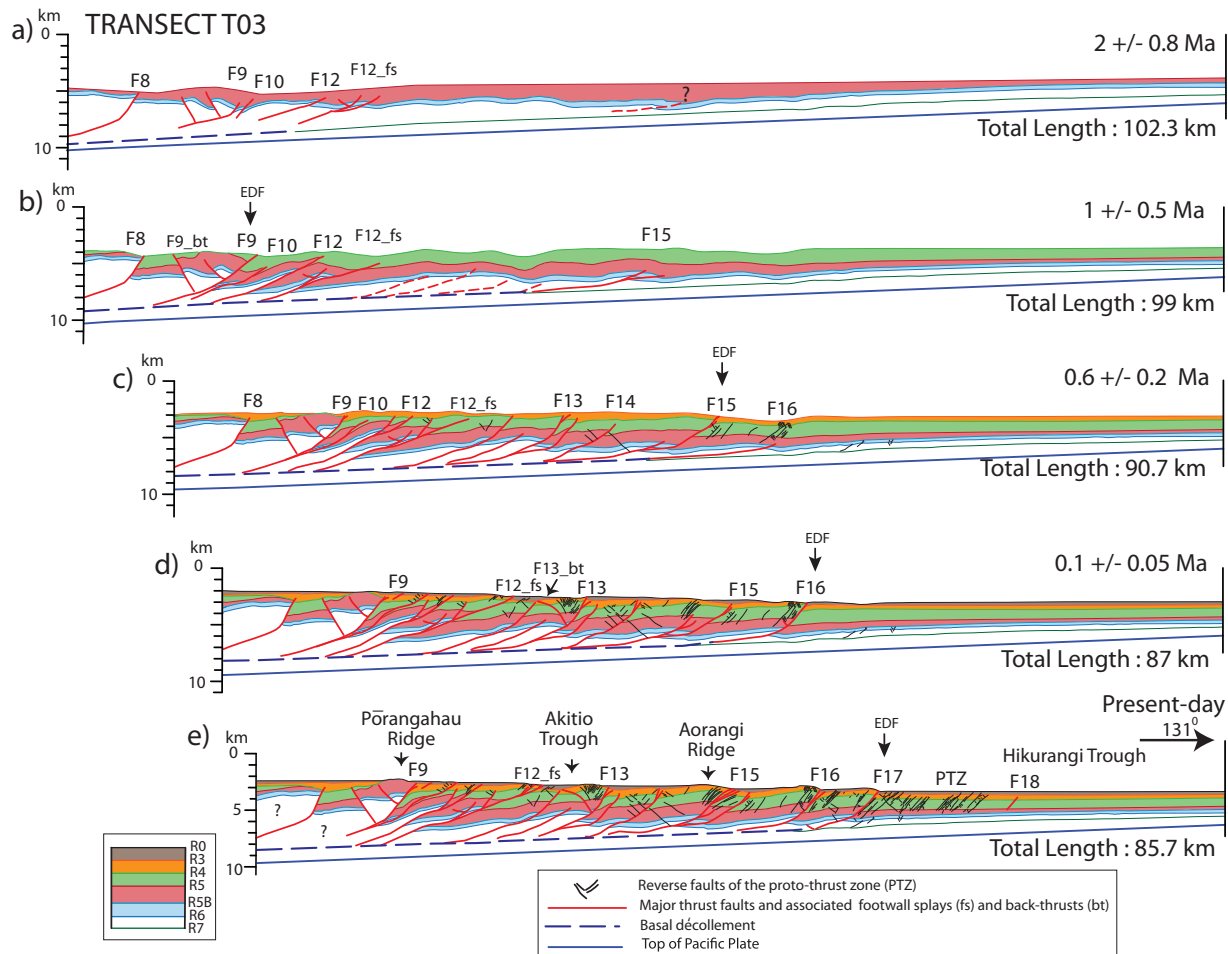
Figure 12. Progressive retro-deformation of Transect T03. (a) Reconstruction at the end of deposition of the sequence below Reflector R5. (b) Reconstruction at the end of deposition of the sequence below Reflector R4. (c) Reconstruction at the end of deposition of the sequence below Reflector R3. (d) Reconstruction during deposition of the sequence R3–R0. (e) Present-day geometry. No vertical exaggeration. Only faults active at each stage are identified by their number. EDF is the emergent deformation front at each stage. See text for details. See Figures S4–S13 in the supporting information file for a more detailed restoration sequence and restoration parameters.

$$f = f_o(e^{-cy})$$

with f = present-day porosity at depth, f_0 = porosity at surface (i.e., the initial porosity), c = porosity-depth coefficient (rate of change of porosity with depth in km^{-1}), and y = depth in m. The parameters used are listed in Figure 2. No adjustments have been incorporated for sea-level and paleo-bathymetric changes.

4.3. Reconstruction of Progressive Deformation in the Restored Transects

The restored geometry of the accretionary wedge in Transects T01, T02, and T03 is shown in Figures 10–12 for four selected stages of the accretionary wedge evolution at 2 ($\pm$0.8) Ma (post-deposition of the sequence topped by Reflector R5); 1 ($\pm$0. 5) Ma (post-deposition of the sequence topped by Reflector R4); 0.6 ($\pm$0.2) Ma (post-deposition of the sequence topped by Reflector R3) and 0.1 ($\pm$0.05) Ma (snapshot of deformation during deposition of the sequence R3–R0).

A more detailed sequence of progressive retro-deformation stages and restoration procedures is provided for Transect T03 in Figures S4–S13 in the supporting information file. These figures are accompanied by a description of kinematic models and parameters used to restore fault separation and folding.

From the oldest stage at 2 ($\pm$0.8) Ma to the present-day, the reconstructed geometry of the wedge displays a number of significant features, as summarized below.

4.3.1. Transect T01

The sedimentary sequence between Reflectors R6 and R5 (Figure 10a) was deposited during deformation of an inner thrust wedge bounded by the emerging thrust fault F7, with piggy-back basins displaying syntectonic growth stratigraphy landward of F7. East of F7, the reconstruction shows a folded outer toe of the wedge with broad anticlines and synclines with wavelength of 3–5 km. Thickness variations and onlaps in the sequence R5–R4 (Figure 10b) identify a wider active portion for the wedge reconstructed during this interval, with propagation of the new thrust faults F8, F9, F10, and F10_fs and associated folding of layers above the fault tips. New blind thrust faults in the lower part of the sequence appear to nucleate east of F10_fs, where they control folding of the outer toe. Further reactivation of inner thrust faults can be reconstructed for faults F1 to F7. At this stage, the emergent deformation front was localized along F7, though the tips of the outermost faults F9, F10, and F10_fs are very close to Reflector R4.

During deposition of the sequence R4–R3 (Figure 10c), there was growth of the outer thrust faults F11, F12, F13, and F14, associated with folding of layers and sets of densely spaced proto-thrusts. F14 was the emergent deformation front at this stage. Note that unit R4–R3 becomes significantly thinner in the piggy-back basins west of fault F10 relative to the outer zones of the wedge, consistent with reactivation of the inner thrust faults (F10–F1).

Deformation during deposition of the sequence R3–R0 between ∼0.6 (±0.2) and 0.1 (±0.05) Ma (Figure 10d) shows the up-section propagation of the already formed thrust faults F14 (emergent deformation front) as well as of F13, F12, and F10, and persistent activity of F7, F8, and F9 with control on seabed morphology. Comparison with the present-day geometry (Figure 10e) shows that propagation of the wide proto-thrust zone east of F14, together with formation of the easternmost thrust fault F16, occurred at a very late stage (perhaps ∼0.1 ± 0.05 Ma).

Variation in length along T01 measured from 2 (±0.8) Ma (original length L_o = 144 km) to the present-day (final length L_f = 122 km) provides an estimate of ∼15% of linear shortening (calculated for this and the other transects as $[(L_f - L_o)/L_o] \times 100$).

4.3.2. Transect T02

Reconstruction of R5 (Figure 11a) reveals an inner wedge deformed by blind thrust faults (F8, F9, F10, F12, and F12_fs) that control lateral variations in the thickness of units and folding of the seafloor. Deformation of the outer toe east of F12_fs is negligible.

Significant thrusting within the wedge occurred by the end of deposition of the sequence R5–R4 (Figure 11b), with propagation of the tips of faults F8, F9, F10, F12, and F12_fs, development of slope basins above the inner imbricates, and outward propagation of the basal décollement with upward splaying of faults F13, F14, and F15. At this stage, the emergent deformation front was localized along F9, with faults east of it remaining blind beneath Reflector R4.

During the following stages (Figures 11c and 11d) deposition of the sequences R4–R3 and R3–R0 was controlled by reactivation of many of the previously formed faults, upward fault tip propagation with associated folding, and no significant eastward advancement of the basal décollement and/or outer deformation front. Reactivation of the inner imbricates (e.g., thrust fault F9) may have controlled deformation of the slope basins, with development of a submarine unconformity, possibly related to mass transport instability (cf. Figure 11c). The latest stage of deformation from about 0.1 (±0.05) Ma to the present-day (Figure 11e) was characterized by propagation of the new frontal thrust faults F16, F17, and F18 ramping from the basal décollement, with development of the outer proto-thrust zone in the upper sequence extending out to Bennett Knoll seamount.

Variation in length along T02 measured from 2 (±0.8) Ma (original length L_o = 100.3 km) to the present-day (final length L_f = 88 km) provides an estimate of ∼12% of linear shortening.

4.3.3. Transect T03

After deposition of the sequence R6–R5, the geometry of the wedge in this transect (Figure 12a) is similar to that shown for Transect T02, with syntectonic thinning of the units west of fault F9; no emergent thrust fault, and little deformation east of fault F12_fs. The following stage, post-deposition of the sequence R5–R4 (Figure 12b), shows some blind faults propagating toward the east (e.g., F15). There was also localized reactivation on the inner thrust faults F8, F9, F9_bt, F10, F12, and F12_fs, associated with onlap and erosion of Reflector R4 in the hanging wall anticline above fault F9 and its back-thrusts.

During deposition of the sequences R4–R3 and R3–R0 (Figures 12c and 12d) the reconstruction shows propagation of the outer faults (F13, F14, F15, and F16) and associated proto-thrusts, coeval with reactivation of

inner thrust faults already formed in the earlier stages. During the latest stage (since about 0.1 ± 0.05 Ma), frontal accretion advanced toward the present deformation front F17, with the further forward propagation of proto-thrust zones (Figure 12e).

Variation in length along T03 measured from 2 (± 0.8) Ma (original length $L_o = 102.3$ km) to the present-day (final length $L_f = 85.7$ km) provides an estimate of linear shortening of $\sim 16\%$.

4.4. Progressive Evolution of the Wedge Interpreted From Restorations

Thrust faults identified as active during progressive deformation of the wedge (Figures 10–12) can be correlated along-strike between Transects T01, T02, and T03. For the present-day geometry, the fault control on the seafloor bathymetry (Figure 1b) makes the map-view correlation relatively straightforward. For the
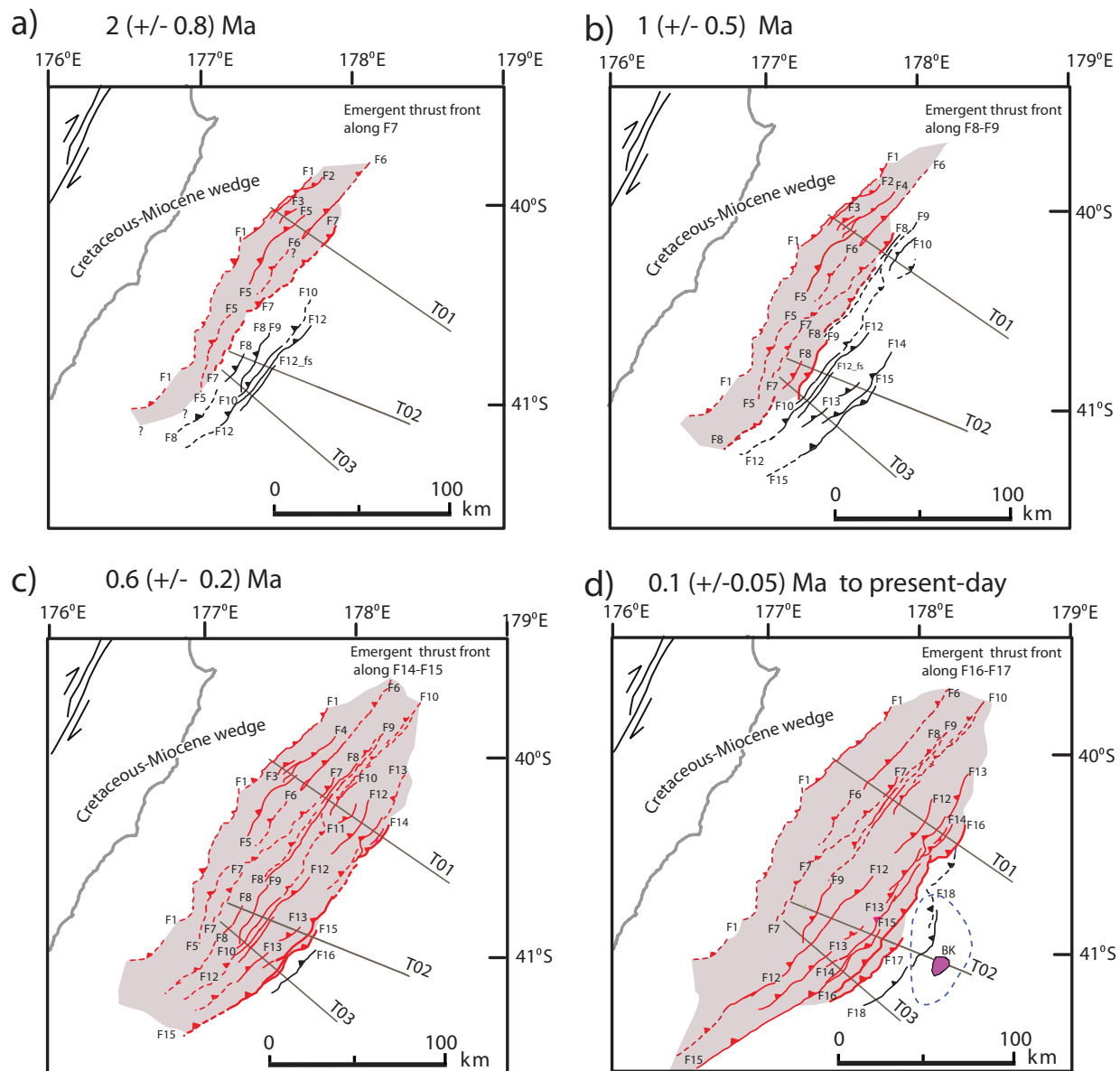
Figure 13. Map view correlations between active thrust faults in the outer accretionary wedge reconstructed from restorations of Transects T01, T02, and T03. (a) Correlations at 2 (± 0.8) Ma. (b) Correlations at 1 (± 0.5) Ma. (c) Correlations at 0.6 (± 0.2) Ma. (d) Correlations from 0.1 (± 0.05) Ma to present-day. Fault numbers as in Figures 10–12. Faults segments interpolated between transects are dashed. For each stage, the gray region is the late Pliocene-Pleistocene portion of the accretionary wedge bounded seaward by the emergent deformation front. Active faults west of the deformation front are in red; blind active faults east of it are in black. The western boundary of the wedge corresponds with the most internal thrust fault (F1) crossed by Transect T01. West of F1 the accretionary wedge comprises Cretaceous to Miocene imbricates and includes active thrust faults not shown in our reconstructions. The Bennett Knoll seamount (BK, with top in purple and base marked by the dashed blue line) is only shown in its present-day position in (d).

retro-deformation steps (a) to (d) in Figures 10–12, the correlation is made possible by the consistency of fault geometry, onset of propagation, and age of activity between the 2-D restorations. Although the present seafloor morphology cannot be used to constrain orientation and trace of individual faults in the restored stages, we can broadly relate the faults at different stages to the present-day ridges, and have used their strike along the seafloor for reconstructing the fault segments interpolated between the three transects. These reconstructions are simplified, but they provide the interpolated along-strike continuity of faults active during progressive deformation of the wedge since 2 (±0.8) Ma, as well as the position and advancement through time of the emergent deformation front (Figure 13).

From the oldest stage (Figure 13a) to the present-day (Figure 13d), our restorations show the progressive addition of an increasingly larger number of active thrust faults within the wedge, with outward propagation of new thrusts coeval with reactivation of faults in inner position. For each restoration stage, forward migration of the wedge is preceded by localization of blind thrust faults east of the emergent deformation front (e.g., F8 to F12 in Figure 13a, F9 to F15 in Figure 13b, F16 in Figure 13c and F18 in Figure 13d), and development of proto-thrust zones. The blind thrust faults ramp up-section from the basal décollement eventually incorporating the earlier proto-thrust faults, and control progressive folding and imbrication of the outer regions of the wedge.

The emergent deformation front is reconstructed in Figure 13 from F7 (at 2 ± 0.8 Ma) to F8–F9 (at 1 ± 0.5 Ma), F14–F15 (at 0.6 ± 0.2 Ma), and F16–F17 (from about 0.1 ± 0.05 Ma to present-day) (cf. Figure 13). Overall the front migrated over a distance of ∼45 km along T01, ∼55 km along T02, and ∼58 km along T03. Thus, over the last 2 (±0.8) Ma, the accretionary wedge widened at a rate of ∼20/30 km/Myr.

5. Discussion

Our geological interpretations and restorations reconstruct the progressive evolution of the outer Hikurangi accretionary wedge in the last 2 (±0.8) Ma. Our analysis introduces a number of assumptions and simplifications (e.g., use of constant velocity intervals for the units separated by marker reflectors in the depth conversions of the SO-191 lines, use of average lithology and porosity values for decompaction, no correction for sea-level changes), and cannot rely on direct dating of the marker reflectors (cf. Figure 2). However, the high-quality resolution of the growth stratigraphy associated with major thrust faults and folds (e.g., Figure 7) provides a solid background for reconstructing the sequence and relative timing of fault activation and folding. Progressive deformation stages reconstructed for the 2-D transects are geometrically admissible and kinematically consistent (Figures 10–12), and allow us to make inferences on modes, amounts, and rates of shortening of the upper plate above the subduction megathrust.

The most significant implications of our study are discussed below.

5.1. Geometry of the Wedge and Inferences on Mechanics of Deformation

Our analysis is based on kinematics only, and it does not incorporate mechanical properties of the deformed sequence (e.g., strength, friction coefficient, fluid overpressure). However, the regional tectonic configuration and the structural geometry can be analyzed in the light of available data from analogue deformation models and similar tectonic settings.

At the regional scale, the structural geometry of Transects T01, T02, and T03 (Figures 3–5) is consistent with the low taper angle (3–4°) of the accretionary wedge that also characterizes the whole southern part of the Hikurangi margin [cf. *Fagereng*, 2011]. Low tapers are inferred to develop above mechanically weak décollements [*Davis et al.*, 1983] and are observed worldwide in low-permeability, clay-rich wedges [*Saffer and Bekins*, 2002], arguably characterized by low friction and/or high fluid overpressures. However, in the upper plate of the Hikurangi subduction margin, complex patterns in fluid circulation and fluid-rock interaction may indicate significant along-strike differences in the fluid-flow regime and fluid pressure [*Reyes et al.*, 2010], thus affecting the mechanical weakness of the interplate megathrust. These differences are particularly relevant to the central segment of the Hikurangi margin because it overlaps the southern transition between the interseismically creeping northern segment and the locked southern segment, thought to be capable of generating large megathrust earthquakes [*Wallace et al.*, 2009].

Defining the parameters that control the variation in space and time of strain release on the subduction interface during the seismic cycle is the topic of ongoing debate [cf. *Fagereng*, 2011; *Bassett et al.*, 2014;

Eberhart-Phillips and Bannister, 2015; *Ellis et al.*, 2015], and is beyond the aims and methodological approach of this study. We can nevertheless infer qualitatively that steepening of the décollement beneath the mid-slope (e.g., T02), the presence of localized asperities at the subduction interface (e.g., Bennett Knoll sea-mount in T02), and the rather irregular spacing between thrust faults [cf. *Koyi and Vendeville*, 2003] suggest that the mechanical strength of the subduction interface may indeed be spatially and temporally heterogeneous within the central section of the margin.

At the smaller scale of the imbricated sedimentary units within the wedge, our geological transects show that significant geometric changes occur below and above Reflectors R5–R5B, which separate the older and more consolidated units of the Hikurangi Plateau sequence from the late Pliocene-Quaternary turbidites deposited in the trench and slope basins (Figure 2). Evidence for these changes include: (1) predominant development of the proto-thrust faults above R5; (2) general difference in trends and rates of separation in the units below R5B relative to the units above (Figure 9), and (3) steepening in fault dip above R5B (Figure 6).

Dip angles of the faults may be particularly sensitive to the lithological and mechanical characteristics of the deformed sequence. In the outermost zones of the three transects, the incipient, small displacement reverse faults of the proto-thrust zones dip preferentially at moderate to steep angles of 40–50° (Figures 6d, 6e, and 6f). Dip angles of 30° are less frequent, though they are considered typical of low-displacement "Andersonian" faults (Coulomb shear fractures) newly propagating across undeformed units [cf. *Sibson*, 2012]. The outer regions east of the primary deformation front are characterized by a regional westward transition from an unconsolidated sedimentary volume undergoing compaction and dewatering under vertical maximum compression to a volume that is in the incipient stage of being incorporated into the accretionary wedge under a regime of horizontal maximum compression [cf. *Morgan et al.*, 2007]. Within this region, conjugate sets of reverse shear deformation bands and fractures dipping at angles >30° have been described for many proto-thrust zones of other accretionary wedges [*Ujiie et al.*, 2004; *Morgan et al.*, 2007]. If the early deformation faults are indeed Coulomb shear faults that formed in a compressional stress regime with subhorizontal maximum compressive stress, their present steep dip angles could be caused by subsequent rotation during superposed shortening [cf. *Morgan et al.*, 2007]. In some proto-thrust zones the steep tectonic fabric is in fact overprinted by shallower dipping structures [*Maltman et al.*, 1993; *Ujiie et al.*, 2004]. We have no evidence for rotation and steepening of Hikurangi proto-thrust faults east of the primary thrust front. Thus, it seems more likely these features initiated as high angle faults and are mechanically analogous to ductile compaction bands that propagated across the unconsolidated, porous sediments [*Bésuelle*, 2001; *Morgan et al.*, 2007].

In contrast with the proto-thrust zones, the major faults of the wedge beneath Reflector R5B (i.e., faults that have propagated across consolidated rock units in the lower part of the sequence) do indeed have the typical, "Andersonian" dip angle of ∼30°. The steepening of the faults across the upper part of the sequence above Reflector R5 (cf. Figures 6a, 6b, 6c, and 7c) may be partly controlled by the pre-existing fabric of the proto-thrusts. This is well illustrated by thrust fault F17 in T02 and T03 (Figures 4b and 5b). The presence of sets of small-scale faults preserved in some fault-bounded panels behind the leading deformation front suggests that many thrust faults propagated across sequences that were already deformed by the high-angle fabric of earlier proto-thrusts.

However, it is also apparent that most of the high angle fault dips in the three transects are associated with fault splays cutting across the youngest stratigraphy. Examples are faults F16, F13, F12, F10 in T01 (Figure 3b), F15, F14 in T02 (Figure 4b), and F16, F15, F13, F12 in T03 (Figure 5b). Sandbox experiments [*Barrier et al.*, 2002] show that when thrusting occurs during sediment accumulation in the footwall (as in our case of basin growth controlled by fault-propagation folding) the propagating fault becomes sealed by sediment and thrusting is accommodated by new fault splays that break up-section at a steeper angle (up to 60°). In these experiments, generation of new fault splays is triggered by the increase in sedimentation rates, and faults that initiated at dip angles of 30° propagate upward at a steeper angle to accommodate the growing pile of sediments stacked in their footwall.

These elements collectively indicate that lithological and mechanical contrasts within the multilayer units, depth-dependent porosity reduction and differential compaction, and varying rates of sediment accumulation controlled by folding strongly affect the style of fault propagation and their geometry.

5.2. Kinematics and Sequence of Wedge Development Reconstructed From Progressive Retro-Deformation

The extremely clear imaging of syntectonic growth stratigraphy (cf. Figure 7) reveals that the structures that deform the present-day outer accretionary prism began to propagate after deposition of the sequence R5B–R5, i.e., post 2 (±0.8) Ma (Figures 10–12). Our analysis is thus limited to a rather short time interval of deformation of the wedge, considering that the Hikurangi subduction began some 20–25 Ma ago. However, field studies, analogue experiments, and theoretical modeling of Coulomb critical wedges [cf. *Dahlen*, 1990; *Graveleau et al.*, 2012] show that wedge construction maintains similar characteristics during repeated episodes of imbrications through time and over different scales. Thus, the sequence and rates of progressive shortening reconstructed for the last 2 (±0.8) Ma of growth of the accretionary wedge may be representative of modes and style fault propagation over longer time intervals, provided there was no major change in the boundary conditions.

The kinematic model of trishear fault-propagation folding adopted in our retro-deformation workflow (Figures 10–12 and supporting information Figures S4–13) makes it possible to link fault growth to folding of layers ahead of the propagating fault tips. Trishear kinematics is consistent with the geometry of folds (Figure 7), as well as with the trends of fault separation decays (Figure 9) [cf. *Hughes and Shaw*, 2014, 2015]. Trishear models have also successfully been used for similar tectonic configurations in the Nankai accretionary prism [*Boston et al.*, 2016].

Considering our restorations of individual transects, the following general progression of deformation characterizes the evolution of the outer accretionary wedge (Figure 13).

1. The oldest deformation stages reconstructed for T01 (Figure 10a), T02 (Figure 11a), and T03 (Figure 12a) depict the frontal wedge at 2 (±0.8) Ma. A number of thrust faults were already present at this stage at the north-western end of the sections, but in both T02 and T03 they remained blind beneath Reflector R5 (Faults F8 to F12_fs in Figures 11a and 12a). The emergent deformation front was localized in a more internal position along F7 and it can only be reconstructed for the northern Transect T01 because the transect is interpreted farther west relative to T02 and T03 (Figure 13a). Though the outer toe of the wedge was relatively undeformed at this stage, incipient shortening is suggested by folding of layers, eventually caused by incipient fault nucleation in the lower stratigraphy (see outer regions of the wedge in Figures 11a and 12a). However, we cannot exclude that the folded geometry of the outer wedge shown in our reconstructions at 2 (±0.8) Ma is an artifact of incomplete retro-deformation, possibly because of unaccounted ductile deformation in the deeper units.

2. Most thrust faults recognized in the present-day wedge formed during deposition of the sequences beneath R4 and R3 (Figures 10b, 10c, 11b, 11c, 12b, and 12c). Thus, from 2 (±0.8) to 0.6 (±0.2) Ma many faults ramped up-section through progressive fault-propagation folding, and breaching of the folded layers during accumulation of ~1000–1500 m of slip on individual faults (cf. Figure 9). Many of these faults evolved from blind to emergent at the end of deposition of Reflector R3, with a regional seaward shifting of ~40 km of the emergent deformation front (Figure 13c).

3. The earliest evidence of proto-thrust fabric reconstructed in the restored transects occurred during fault propagation across the sequence topped by Reflector R3 (Figure 3). However, lack of evidence of older fabrics is likely caused by poor seismic resolution within the folded and imbricated units, as well as by the potential incorporation of the early low-displacement faults into the newly propagating thrust faults. The incorporation of early developed proto-thrust fabric by subsequent fault imbrication is very clear in the outer Hikurangi accretionary wedge, and it has been noted in other accretionary wedges worldwide [e.g., *Morgan and Karig*, 1995; *Morgan et al.*, 2007].

4. In all transects, forward-advancing deformation in the outer wedge was synchronous with persistent reactivation of earlier faults located more internally. The largest of these out-of-sequence faults (e.g., F7 and F9) have locally controlled the morphology of the seafloor since at least 2 (±0.8) Ma, and they continue to do so at present (e.g., Paoanui and Pōrangahau Ridges).

5. The advancement of the basal décollement through time is heralded by the propagation of blind thrust faults ahead of the leading thrust front. This advancement appears to be differential from north to south, and larger for the region crossed by Transects T02 and T03 relative to T01 (Figure 13).

The sequence of deformation outlined above has regional-scale implications for the structural evolution and propagation through time of an accretionary wedge. In particular, our restorations suggest that forward

propagation of the basal décollement and discrete thrusting are preceded by early stages of bulk shortening at the outer toe of the wedge, with development of pervasive sets of proto-thrusts. Once the basal décollement propagates, strain localization occurs and thrust faults ramp up-section (eventually incorporating the earlier deformation fabric) in a relatively short time interval (~1.0–1.5 Ma in our case). The reverse separation accrued on faults F11 to F17 varies from ≥1500 to ≤300 m (Figure 9), with slip rates in the range of ~1–9 mm/year if averaged over the time of fault growth reconstructed from restorations (Figures 10–12). Slip rates of individual faults are thus highly variable across the wedge, with the highest values potentially characterizing the newly propagating frontal thrusts (e.g., F16, F17) during the relatively short time interval since their inception (~0.1 ± 0.05 Ma). Creation of new faults within the wedge conforms to a general sequence of outward fault propagation, but faults already formed in more internal positions also undergo reactivation ("out-of-sequence" thrusting) [cf. *Morley*, 1988]. Renewed activity on the inner faults can be interpreted as a mechanical adjustment that thickens the wedge and maintains its critical taper angle [*Platt*, 1990]. Differential advancement of the wedge (see e.g., southern Transects T02 and T03 relative to the northern Transect T01 in our study region) may be related to increased weakness of the basal décollement [*Wallace et al.*, 2003] and/or to a possible southward increase in fluid pressure in the region [*Fagereng and Ellis*, 2009; *Reyners and Eberhart-Phillips*, 2009]. However, asynchronous episodes of rapid wedge advancement along the margin may also be controlled by other factors, such as along-strike changes in sediment accumulation, or potential subduction of asperities over time (e.g., seamounts, see Transect T02).

5.3. Amount and Rates of Shortening Derived From Restorations

Linear shortening measured along Transects T01, T02, and T03 is respectively: −22 km (15% over a length of 122 km), −15 km (12% over a length of 100.3 km), and −16.6 km (16% over a length of 102.3 km). These values represent a minimum estimate of the change in length on the plane of the section consequent on macroscopic thrusting and folding since 2 (±0.8) Ma.

The restorations shown in Figures 10–12 are nonunique, and our results depend on the choice of restoration workflow and kinematic models, as described in section 4 and supporting information Figures S4–S13. These shortening values may thus be affected by unquantifiable errors resulting from multiple factors (e.g., parameters used for trishear restoration; retro-deformation of units to a nonhorizontal datum; undetected deformation below the resolution of seismic data; components of shortening away from the plane of the 2-D sections). The larger linear shortening measured for T01 partly reflects the wider length of this transect across-strike into the more internal regions of the wedge relative to T02 and T03.

Shortening estimates derived from our analysis are comparable to those of *Barnes and Mercier de Lépinay* [1997], who calculated 12.5% shortening along different and older seismic profiles in the same region. They are also comparable to values of 15–33 km of shortening over a longer time interval of 5 Myr estimated by *Nicol and Beavan* [2003] from bed length restoration to the horizontal from the same region of the margin.

Restorations performed using 2-D linear balancing of fault-imbricated and folded beds in outer regions of other accretionary prisms [e.g., *Morgan and Karig*, 1995; *Moore et al.*, 2011] also show that discrete faulting and folding at the outer toe of the prism only accounts for low amounts of shortening (1.1 km over a length of 10.5 km, i.e., ~9.5% in the reconstruction of *Morgan and Karig* [1995] and 1.3–2 km over a length of ~23 km, i.e., ~5.6–8.6% in the reconstructions of *Moore et al.* [2011]).

When inferring deformation rates from restored units, estimates depend critically on the age of the stratigraphic markers and unfortunately we have no precise dating for our markers (cf. Figure 2). If Reflector R5 has an age of 2 (±0.8) Ma, the average shortening rates of the outer wedge (calculated from a maximum age of 2.8 Ma and a minimum age of 1.2 Ma to the present-day) can be bracketed in the range of ~8–18 mm/yr for T01, 4–10 mm/yr for T02, and 6–14 mm/yr, for T03. These values compare with an average late Quaternary (0.4 ± 0.1 Ma) rate of 12 ± 3 mm/yr estimated by *Barnes and Mercier de Lépinay* [1997] for the same region. However, our reconstructions suggest that shortening rates may vary through time (cf. variations in length between stages (a), (b), (c), (d) and (e) in Figures 10–12). Even allowing for larger, time-dependent rates (e.g., up to ~21 mm/yr between reconstructions in Figures 12b and 12c for T03 if calculated for the shortest time interval of 0.4 Myr), these rates are significantly lower than the margin-normal plate convergence rates of ~31–40 mm/yr calculated for this part of the margin [*Wallace et al.*, 2004, 2012].

The general low values of shortening imparted by macroscopic brittle faults and folds within the wedge and the discrepancy between shortening rates from restored 2-D transects and plate convergence rates can be analyzed in the light of the following factors.

Restorations only remove 2-D deformation accommodated by thrust faulting and fault-propagation folding above the basal décollement. Though we have been able to interpolate fault continuity between the three transects (Figure 13), the relatively large spacing between seismic lines and the lack of a 3-D seismic volume make it impossible to reconstruct the 3-D geometry of the wedge for this study. Thus, we may miss components of shortening away from the plane of the sections, also considering the small obliquity of the regional thrust faults relative to the plate convergence vector (Figure 1a).

The partitioning between shortening accommodated by faulting/folding versus pervasive shortening of sedimentary units (e.g., porosity reduction by diagenetic compaction or tectonic layer-parallel shortening, pressure solution cleavage) is a long debated problem in section balancing [*Hossack*, 1979]. In fact, penetrative deformation causes significant volume changes, in contrast with the basic assumption of section balancing, requiring area conservation (plane strain) within the deformed region above the basal décollement. Field studies [*Fisher and Coward*, 1982; *Cooper et al.*, 1983; *Mitra*, 1994], and laboratory experiments [*Koyi*, 1995; *Koyi et al.*, 2004] suggest that significant components of shortening (up to 30–50%) are accommodated by processes that are unresolvable at the scale of seismic sections, and therefore remain undetected in regional reconstructions based on seismic data. For the Nankai accretionary prism, *Moore et al.* [2011] estimate that shortening reconstructed from discrete faulting and folding on macroscopic structures accounts for only 24–35% of the total horizontal shortening across the outer wedge, with the remaining part accommodated by volumetric reduction in porosity. Several studies, as well as drilling data, show that shortening of porous, unconsolidated sediments at the toe of accretionary wedges occurs by distributed, ductile shear, and small scale faulting that precede thrust fault propagation [*Karig and Lundberg*, 1990; *Owens*, 1993; *Morgan and Karig*, 1995; *Henry et al.*, 2003]. In these regions, an estimated 20–50% of total shortening remains unaccounted by restoration of seismically resolvable faults [*Morgan et al.*, 1994]. The subseismic component can be revealed by volumetric strain analyses based on vertical thickening of sediments [*Morgan and Karig*, 1995], or anisotropy of physical parameters (e.g., P-wave velocity, magnetic susceptibility) to measure lateral porosity reduction [*Brueckmann et al.*, 1993; *Moore et al.*, 2011]. In our analysis, we have only corrected for vertical compaction caused by the sedimentary load, using the *Sclater and Christie* [1980] relationship. However, our restorations show a landward increase in the thickness of stratigraphic units above R5B (Figure 8) that may incorporate a component of vertical thickening of sediments caused by horizontal shortening. The quantification of this component is difficult, because it needs to discriminate thickness variations associated with onlap of units onto the W-tilted Hikurangi Plateau, as well as thickness perturbations localized in the hanging wall and footwall of thrust faults (Figure 8). At this stage, we are unable to quantify the amount of layer-parallel tectonic shortening in the trench sediments that were progressively accreted above the décollement, though we suspect that it may represent a large percentage of total shortening (up to ∼40%) if values measured in other accretionary wedges worldwide [*Moore et al.*, 2011] can be also applied to the Hikurangi margin.

Note also that additional components of interplate convergence can be accommodated ahead of the leading thrust front by shear along the forward propagating basal décollement [e.g., *Morgan and Karig*, 1995], as well as by cumulative reverse separation across the pervasive system of closely spaced proto-thrust faults that extend for a width of up to 25 km east of the frontal thrust.

For the central Hikurangi region, *Nicol and Wallace* [2007] considered that only 15% of margin-normal plate convergence since 1.5 Ma is recorded by geological faults and folds across the Australian Plate (excluding the frontal 50 km of the accretionary wedge). These authors concluded that 85% of the 30–40 mm/yr (Figure 1a) convergence rate (i.e., 25–34 mm/yr) is accommodated along the subduction thrust and distributed within the outer accretionary wedge. These results make it unlikely that significant components of shortening unaccounted by our restorations are partitioned into more internal regions of the wedge (cf. Figure 13) and/or on upper plate faults onshore. However, in the more internal part of our transects (west of Paoanui and Pōrangahau Ridges), seismic resolution is generally poor, and alternative interpretations of the geometry of imbricated units beneath Reflector R5B may include the development of blind duplexes above the basal décollement (A. Plaza Faverola et al., in preparation), potentially resulting in additional components of shortening.

6. Conclusions

This paper presents the interpretation and progressive retro-deformation of three geological transects across the outer accretionary wedge of the central Hikurangi margin. Our analysis takes advantage of the high-quality resolution of growth stratigraphy controlled by faulting in the seismic lines, enabling us to track the progressive evolution of the wedge since 2 ($\pm$0.8) Ma.

Our study shows that shortening of the outer units occurred by initial development of pervasive, small-scale proto-thrust faults, followed by propagation of the larger-scale thrust faults that ramp up-section from the basal décollement, eventually incorporating the pre-existing proto-thrusts. Fault propagation and folding of layers above the fault tips are consistent with trishear kinematic models, and result in a strong control on growth stratigraphy within the syntectonic units. Slip rates of individual faults appear to be highly variable ($\sim$1–9 mm/year) across the wedge and over time, with the highest values measured for the youngest frontal thrusts that may have propagated since $\sim$0.1 $\pm$ 0.05 Ma. The reconstructed geometric configuration defines a low-taper wedge that has widened at a rate of 20–30 km/Myr since 2.0 ($\pm$0.8) Ma, above a relatively weak megathrust interface. The critical taper angle has been maintained by persistent out-of-sequence reactivation of the inner thrust faults, coeval with forward propagation of the leading deformation front.

The cumulative shortening and the average shortening rates ($\leq$18 mm/yr) since 2 ($\pm$0.8) Ma estimated from restorations account only for the components of deformation accommodated by faults and fault-propagation folding above the basal décollement since 2 ($\pm$0.8) Ma. These values represent only $\sim$50% of the total shortening imposed by plate convergence, with the remaining components possibly accommodated by distributed mesoscale and microscale deformation within the wedge, outer décollement zone, and proto-thrust zones.

Our development and use of progressive restoration techniques for the offshore Hikurangi margin is innovative, and makes it possible to reconstruct stages of progressive shortening of sedimentary units deposited during fault-propagation folding. The general sequence of deformation outlined for this region of the Hikurangi margin may be applicable to other accretionary wedges with similar characteristics worldwide.

References

Allmendinger, R. W. (1998), Inverse and forward numerical modeling of trishear fault-propagation folds, *Tectonics*, *17*, 640–656.

Allmendinger, R. W., T. Zapata, R. Manceda, and F. Dzelalija (2004), Trishear kinematic modeling of structures, with examples from the Neuquén Basin, Argentina, in *Thrust Tectonics and Hydrocarbon Systems, Am. Assoc. Pet. Geol. Mem. 82*, edited by K. R. McKlay, pp. 356–371, Am. Assoc. of Pet. Geol., Tulsa, Okla.

Ballance, P. F. (1976), Evolution of the Upper Cenozoic magmatic arc and plate boundary in northern New Zealand, *Earth Planet. Sci. Lett.*, *28*, 356–370.

Barker, D. H. N., R. Sutherland, S. Henrys, and S. Bannister (2009), Geometry of the Hikurangi subduction thrust and upper plate, North Island, New Zealand, *Geochem. Geophys. Geosyst.*, *10*, Q02007, doi:10.1029/2008GC002153.

Barnes, P. M., and B. Mercier de Lépinay (1997), Rates and mechanics of rapid frontal accretion along the very obliquely convergent southern Hikurangi margin, New Zealand, *J. Geophys. Res.*, *102*, 24,931–24,952.

Barnes, P. M., B. Mercier de Lépinay, J.-Y. Collot, J. Delteil, and J.-C. Audru (1998), Strain partitioning in the transition area between oblique subduction and continental collision, Hikurangi margin, New Zealand, *Tectonics*, *17*, 534–557.

Barnes, P. M., G. Lamarche, J. Bialas, S. Henrys, I. Pecher, G. L. Netzeband, J. Greinert, J. J. Mountjoy, K. Pedley, and G. Crutchley (2010), Tectonic and geological framework for gas hydrates and cold seeps on the Hikurangi subduction margin, New Zealand, *Mar. Geol.*, *272*, 26–48, doi:10.1016/j.margeo.2009.03.012.

Barnes, P. M., F. C. Ghisetti, S. Ellis, D. H. N. Barker, F. Henrys, and S. Henrys (2014), Megathrust propagation and accretionary wedge development at the front of a sediment-rich subduction system, central Hikurangi margin, New Zealand, *AGU 2014 Abstract and poster*.

Barrier, L., T. Nalpas, D. Gapais, J. N. Proust, A. Casas, and S. Bourquin (2002), Influence of syntectonic sedimentation on thrust geometry. Field examples from the Iberian Chain (Spain) and analogue modelling, *Sediment. Geol.*, *146*, 91–104.

Bassett, D., R. Sutherland, and S. Henrys (2014), Slow wavespeeds and fluid overpressure in a region of shallow geodetic locking and slow slip, Hikurangi subduction margin, New Zealand, *Earth Planet. Sci. Lett.*, *389*, 1–13, doi:10.1016/j.epsl.2013.12.021.

Beanland, S., A. Melhuish, A. Nicol, and J. Ravens (1998), Structure and deformation history of the inner forearc region, Hikurangi subduction margin, New Zealand, *N. Z. J. Geol. Geophys.*, *41*, 325–342.

Beavan, J., P. Tregoning, M. Bevis, T. Kato, and C. Meertens (2002), Motion and rigidity of the Pacific Plate and implications for plate boundary deformation, *J. Geophys. Res.*, *107*(B10), 2261, doi:10.1029/2001JB000282.

Bésuelle, P. (2001), Compacting and dilating shear bands in porous rock: Theoretical and experimental conditions, *J. Geophys. Res.*, *106*, 13,435–13,442.

Boston, B., G. F. Moore, M. J. Jurado, and H. Sone (2016), Deformation of the Nankai Trough inner accretionary prism: The role of inherited structures, *Geochem. Geophys. Geosyst.*, *17*, 485–500, doi:10.1002/2015GC006185.

Brandes, C., and D. C. Tanner (2014), Fault-related folding: A review of kinematic models and their application, *Earth Sci. Rev.*, *138*, 352–370.

Brueckmann, W., K. Moran, and E. Taylor (1993), Acoustic anisotropy and microfabric development in accreted sediments from the Nankai Trough, *Proc. Ocean Drill. Program Sci. Results*, *131*, 221–233.

Burgreen-Chan, B., E. K. Meisling, and S. Graham (2015), Basin and petroleum system modelling of the East Coast Basin, New Zealand: A test of overpressure scenarios in a convergent margin, *Basin Res.*, doi:10.1111.bre.12121.

Cole, J., and K. Lewis (1981), Evolution of the Taupo-Hikurangi subduction system, *Tectonophysics*, *72*(1–2), 1–21, doi:10.1016/0040-1951(81)90084-6.

Colletta, B., J. Letouzey, R. Pinedo, J. F. Ballard, and P. Balé (1991), Computerized X-ray tomography analysis of sandbox models: Examples of thin-skinned thrust systems, *Geology*, *19*, 1063–1067.

Cooper, M. A., M. R. Garton, and J. R. Hossack (1983), The origin of the Basse Normandie duplex, Boulonnais, France, *J. Struct. Geol.*, *5*(2), 139–152.

Dahlen, F. (1990), Critical taper model of fold-and-thrust belts and accretionary wedges, *Annu. Rev. Earth Planet. Sci.*, *18*, 55–99.

Davis, D. J., J. Suppe, and F. A. Dahlen (1983), Mechanics of folds and thrust belts and accretionary wedges, *J. Geophys. Res.*, *88*, 1153–1172.

Davy, B. R., K. Hoernle, and R. Werner (2008), Hikurangi Plateau: Crustal structure, rifted formation and Gondwana subduction history, *Geochem. Geophys. Geosyst.*, *9*, Q07004, doi:10.1029/2007GC001855.

DeMets, C., R. G. Gordon, D. F. Argus, and S. Stein (1994), Effects of recent revisions to the geomagnetic reversal time scale on estimates of current plate motions, *Geophys. Res. Lett.*, *21*, 2191–2194.

Eberhart-Phillips, D., and S. Bannister (2015), 3-D imaging of the northern Hikurangi subduction zone, New Zealand: Variations in subducted sediment, slab fluids and slow slip, *Geophys. J. Int.*, *201*, 838–855, doi:10.1093/gji/ggv057.

Ellis, S., A. Fagereng, D. Barker, S. Henrys, D. Saffer, L. Wallace, C. Williams, and R. Harris (2015), Fluid budgets along the northern Hikurangi subduction margin, New Zealand, the effect of a subducting seamount on fluid pressure, *Geophys. J. Int.*, *202*, 277–297, doi:10.1093/gji/ggv127.

Erslev, E. A. (1991), Trishear fault-propagation folding, *Geology*, *19*, 617–620.

Fagereng, Å. (2011), Wedge geometry, mechanical strength, and interseismic coupling of the Hikurangi subduction thrust, New Zealand, *Tectonophysics*, *507*, 26–30, doi:10.1016/j.tecto.2011/05.004.

Fagereng, Å., and S. Ellis (2009), On factors controlling the depth of interseismic coupling on the Hikurangi subduction interface, New Zealand, *Earth Planet. Sci. Lett.*, *278*, 120–130, doi:10.1016/j.epsl.2008.11.033.

Fisher, M. W., and M. P. Coward (1982), Strains and folds within thrust sheets: An analysis of the Heilam Sheet, Northwest Scotland, *Tectonophysics*, *88*, 291–312.

Gibbs, A. D. (1983), Balanced cross-section construction from seismic sections in areas of extensional tectonics, *J. Struct. Geol.*, *141*, 121–129.

Graveleau, F., J. Malavieille, and S. Dominguez (2012), Experimental modelling of orogenic wedges: A review, *Tectonophysics*, *538–540*, 1–66, doi:10.1016/j.tecto.2012.01.027.

Groshong, R. H., Jr. (2006), *3-D Structural Geology*, 2nd ed., 400 pp., Springer, Berlin Heidelberg, N. Y.

Hardy, S., and M. Ford (1997), Numerical modeling of trishear fault-propagation folding, *Tectonics*, *16*, 841–854.

Henry, P., L. Jouniaux, E. J. Screaton, S. Hunze, and D. M. Saffer (2003), Anisotropy of electrical conductivity record of initial strain at the toe of the Nankai accretionary wedge, *J. Geophys. Res.*, *108*(B9), 2407, doi:10.1029/2002JB002287.

Hossack, J. R. (1979), The use of balanced cross-sections in the calculation of orogenic contraction: A review, *J. Geol. Soc. London*, *136*, 705–711.

Hughes, A. N., and J. H. Shaw (2014), Fault displacement-distance relationships as indicators of contractional fault-related folding style, *Am. Assoc. Pet. Geol. Bull.*, *98*(2), 227–251, doi:10.1306/05311312006.

Hughes, A. N., and J. H. Shaw (2015), Insights into the mechanics of fault-propagation folding styles, *Geol. Soc. Am. Bull.*, *127*(11–12), 1752–1765, doi:10.1130/B31215.1

Karig, D. E., and N. Lundberg (1990), Deformation bands from the toe of the Nankai accretionary prism, *J. Geophys. Res.*, *95*, 9099–9109.

Koyi, H. (1995), Mode of internal deformation in sand wedges, *J. Struct. Geol.*, *17*(2), 293–300.

Koyi, H. A., and B. C. Vendeville (2003), The effect of decollement dip on geometry and kinematics of model accretionary wedges, *J. Struct. Geol.*, *25*, 1445–1450.

Koyi, H. A., M. Sans, A. Teixell, J. Cotton, and H. Zeyen (2004), The significance of penetrative strain in the restoration of shortened layers—Insights from sand models and the Spanish Pyrenees, in *Thrust Tectonics and Hydrocarbon Systems, Am. Assoc. Pet. Geol. Mem. 82*, edited by K. R. McKlay, pp. 207–222, Am. Assoc. of Pet. Geol., Tulsa, Okla.

Lamb, S. (2011), Cenozoic tectonic evolution of the New Zealand plate-boundary zone: A paleomagnetic perspective, *Tectonophysics*, *509*(3–4), 135–164, doi:10.1016/j.tecto.2011.06.005.

Lewis, K. B., and H. M. Pantin (2002), Channel-axis, overbank and drift sediment waves in the southern Hikurangi Trough, New Zealand, *Mar. Geol.*, *192*, 123–151.

Lewis, K. B., and J. R. Pettinga (1993), The emerging, imbricated frontal wedge of the Hikurangi Margin, in *South Pacific Sedimentary Basins (Sedimentary Basins of the World, 2)*, edited by P. F. Balance, pp. 225–250, Elsevier, Amsterdam.

Lewis, K. B., J.-Y. Collot, and S. E. Lallemand (1998), The dammed Hikurangi Trough: A channel-fed trench blocked by subducting seamounts and their wake avalanches (New Zealand-France GeodyNZ Project), *Basin Res.*, *10*(4), 441–468, doi:10.1046/j.1365-2117.1998.00080.x.

Lundberg, N., and J. C. Moore (1986), Macroscopic structural features in Deep Sea Drilling Project cores from forearcs, *Geol. Soc. Am. Mem.*, *166*, 13–44.

Maltman, A. J., T. Byrne, D. E. Karig, and S. Lallemant (1993), Deformation at the toe of an active accretionary prism: Synopsis of results from ODP Leg 131, Nankai, SW Japan, *J. Struct. Geol.*, *15*, 949–964.

Midland Valley (2014−2015), *MOVE* software, Glasgow, U. K. [Available at http://www.mve.com].

Mitra, G. (1994), Strain variation in thrust sheets across the Sevier fold-and-thrust belt (Idaho-Utah-Wyoming): Implications for section restoration and wedge taper evolution, *J. Struct. Geol.*, *16*(4), 585–602.

Moore, J. C. (1989), Tectonics and hydrogeology of accretionary prisms: Role of the decollement zone, *J. Struct. Geol.*, *11*, 95–106.

Moore, G. F., D. Saffer, M. Studer, and P. Costa Pisani (2011), Structural restoration of thrusts at the toe of the Nankai Trough accretionary prism off Shikoku Island, Japan: Implications for dewatering processes, *Geochem. Geophys. Geosyst.*, *12*, Q0AD12, doi:10.1029/2010GC003453.

Morgan, J. K., and D. E. Karig (1995), Decollement processes at the Nankai accretionary margin, southern Japan: Propagation, deformation and dewatering, *J. Geophys. Res*, *100*, 15,221–15,231.

Morgan, J. K., D. E. Karig, and A. Maniatty (1994), The estimation of diffuse strains in the toe of the western Nankai accretionary prism: A kinematic solution. *J. Geophys. Res.*, *99*, 7019–7032.

Morgan, J. K., E. B. Sunderland, and M. V. S. Ask (2007), Deformation and mechanical strength of sediments at the Nankai subduction zone: implications for prism evolution and décollement initiation and propagation, in *The Seismogenic Zone of Subduction Thrust Faults*, edited by T. H. Dixon and J. C. Moore, pp. 210–247, Columbia Univ. Press, N. Y.

Morley, C. K. (1988), Out-of-sequence thrusts, *Tectonics*, 7(3), 539–561, doi:10.1029/TC007i003p00539.

Nicol, A., and J. Beavan (2003), Shortening of an overriding plate and its implications for slip on a subduction thrust, central Hikurangi margin, New Zealand, *Tectonics*, 22(6), 1070, doi:10.1029/2003TC001521.

Nicol, A., and L. M. Wallace (2007), Temporal stability of deformation rates: Comparison of geological and geodetic observations, Hikurangi subduction margin, New Zealand, *Earth Planet. Sci. Lett.*, 258, 397–413, doi:10.1016/j.epsl.2007.03.039.

Nicol, A., C. Mazengarb, F. Chanier, G. Rait, C. Uruski, and L. Wallace (2007), Tectonic evolution of the Hikurangi subduction margin, New Zealand, since the Oligocene, *Tectonics*, 26, TC4002, doi:10.1029/2006TC002090.

Owens, W. H. (1993), Magnetic fabric studies of samples from Hole 808C, Nankai Trough, *Proc. Ocean Drill. Program Sci. Results, Part B*, 131, 301–310.

Pettinga, J. R. (1982), Upper Cenozoic structural history, coastal southern Hawke's Bay, New Zealand, *N. Z. J. Geol. Geophys.*, 25, 149–191.

Platt, J. (1990), Thrust mechanics in highly overpressured accretionary wedges, *J. Geophys. Res.*, 95, 9025–9034.

Plaza-Faverola, A., D. Klaeschen, P. Barnes, I. Pecher, S. Henrys, and J. Mountjoy (2012), Evolution of fluid expulsion and concentrated hydrate zones across the southern Hikurangi subduction margin, New Zealand: An analysis from depth migrated seismic data, *Geochem. Geophys. Geosyst.*, 13, Q08018, doi:10.1029/2012GC004228.

Reyes, A. G., B. W. Christenson, and K. Faure (2010), Sources of solutes and heat in low-enthalpy mineral waters and their relation to tectonic setting, New Zealand, *J. Volcanol. Geotherm. Res.*, 192, 177–141, doi:10.1016/j.volgeores.2010.02.015.

Reyners, M., and D. Eberhart-Phillips (2009), Small earthquakes provide insight into plate coupling and fluid distribution in the Hikurangi subduction zone, New Zealand, *Earth Planet. Sci. Lett.*, 282(1–4), 299–305, doi:10.1016/j.epsl.2009.03.034.

Saffer, D. M., and B. A. Bekins (2002), Hydrologic controls on the morphology and mechanics of accretionary wedges, *Geology*, 30, 271–274.

Schreurs, G., et al. (2006), Analogue benchmarks of shortening and extension experiments, in *Analogue and Numerical Modelling of Crustal-Scale Processes, Geol. Soc. of London Spec. Publ. 253*, edited by S. J. H. Buiter and G. Schreurs, pp. 1–27, Geol. Soc. of Am., London, U. K.

Sclater, J. G., and P. A. F. Christie (1980), Continental stretching: An explanation of the post mid-Cretaceous subsidence of central North Sea Basin, *J. Geophys. Res.*, 85, 3711–3739.

Shaw, J. H., E. Novoa, and C. D. Connors (2004), Structural controls on growth stratigraphy in contractional fault-related folds, in *Thrust Tectonics and Hydrocarbon Systems, Am. Assoc. Pet. Geol. Mem. 82*, edited by K. R. McKlay, pp. 400–412, Am. Assoc. of Pet. Geol., Tulsa, Okla.

Sibson, R. H. (2012), Reverse fault rupturing: Competition between non-optimal and optimal fault orientations, in *Faulting, Fracturing and Igneous Intrusion in the Earth's Crust, Geol. Soc. of London Spec. Publ. 367*, edited by D. Healy, et al., pp. 39–50, Geol. Soc. of Am., London, U. K., doi:10.1144/SP367.4.

Sitchler J. C., D. M. Fisher, T. W. Gardner, and M. Protti (2007), Constraints on inner forearc deformation from balanced cross sections, Fila Costeña thrust belt, Costa Rica, *Tectonics*, 26, TC6012, doi:10.10129/2006TC001949.

Storti, F., and K. McClay (1995), The influence of sedimentation on the growth of thrust wedges in analogue models, *Geology*, 23, 999–1002.

Ujiie, K., A. J. Maltman, and M. Sanchez-Gómez (2004), Origin of deformation bands in argillaceous sediments at the toe of the Nankai accretionary prism, southwest Japan, *J. Struct. Geol.*, 26, 221–231.

Von Huene, R. (1986), To accrete or not accrete, that is the question, *Geol. Rundsch.*, 75, 1–15.

Walcott, R. I. (1998), Modes of oblique compression: Late Cenozoic tectonics of the South Island of New Zealand, *Rev. Geophys.*, 36, 1–26.

Wallace G., J. C. Moore, and C. G. DiLeonardo (2003), Controls on localization and densification of a modern décollement: Northern Barbados accretionary prism, *Geol. Soc. Am. Bull.*, 115(3), 288–297.

Wallace, L. M., J. Beavan, R. McCaffrey, and D. Darby (2004), Subduction zone coupling and tectonic block rotations in the North Island, New Zealand, *J. Geophys. Res.*, 109, B12406, doi:10.1029/2004JB003241.

Wallace, L. M., et al. (2009), Characterizing the seismogenic zone of a major plate boundary subduction thrust: Hikurangi margin, New Zealand, *Geochem. Geophys. Geosyst.*, 10, Q10006, doi:10.1029/2009GC002610.

Wallace, L., P. M. Barnes, J. Beavan, R. Van Dissen, N. Litchfield, J. Mountjoy, R. Langridge, G. Lamarche, and N. Pondard (2012), The kinematics of a transition from subduction to strike-slip: An example from the central New Zealand plate boundary, *J. Geophys. Res.*, 117, B02405, doi:10.1029/2011JB008640.

Wallace, L. M., S. C. Webb, Y. Ito, K. Mochizuki, R. Hino, S. Henrys, S. Y. Schwartz, and A. F. Sheehan (2016), Slow slip near the trench at the Hikurangi subduction zone, New Zealand, *Science* 352(6286), 701–704, doi:10.1126/science.aaf2349.

Wells, P. E. (1990), Porosities and seismic velocities of mudstones from Wairarapa and oil wells of North Island, New Zealand, and their use in determining burial history, *N. Z. J. Geol. Geophys.*, 33(1), 29–39.

Williams, G., and T. Chapman (1983), Strains developed in the hanging-walls of thrusts due to their slip/propagation rate: A dislocation model, *J. Struct. Geol.*, 5(6), 563–571, doi:10.1016/0191-8141(83)90068-8.

Yamada, Y., K. Baba, and T. Matsuoka (2006), Analogue and numerical modelling of accretionary prisms with a décollement in sediments, in *Analogue and Numerical Modelling of Crustal-Scale Processes, Geol. Soc. of London Spec. Publ., 253* edited by S. J. H. Buiter and G. Schreurs, pp. 169–183, Geol. Soc. of Am., London, U. K.